remote sensing

MDPI

Article

Landslide Mapping and Causes of Landslides in the China–Nepal Transportation Corridor Based on Remote Sensing Technology

Shufen Zhao [1,2], Runqiang Zeng [1,2,*], Zonglin Zhang [1,2], Xingmin Meng [1,2], Tianjun Qi [1,2], Zhao Long [1,2], Weiwei Guo [1,2] and Guojun Si [1,2]

1 School of Earth Sciences, Lanzhou University, Lanzhou 730000, China; zhaoshf21@lzu.edu.cn (S.Z.); zhangzl2016@lzu.edu.cn (Z.Z.); 220220903631@lzu.edu.cn (Z.L.)
2 Technology & Innovation Centre for Environmental Geology and Geohazards Prevention, Lanzhou 730000, China
* Correspondence: zengrq@lzu.edu.cn

Abstract: The China–Nepal Transportation Corridor is vital to the country's efforts to build a land trade route in South Asia and promote the Ring-Himalayan Economic Cooperation Belt. Due to the complex geological structure and topographical environment of the Qinghai–Tibet Plateau, coupled with the impact of climate change, the frequent occurrence of geological disasters has increased the operational difficulty of the China–Nepal Highway and the construction difficulty of the China–Nepal Railway. However, to date, there has been no systematic study of the spatial distribution of landslides along the entire route within the area, the factors influencing landslides at different scales, or the causes of landslides under different topographic backgrounds. There is an even greater lack of research on areas threatened by potential landslides. This study comprehensively applies remote sensing, mathematical statistics, and machine learning methods to map landslides along the China–Nepal transportation corridor, explore the influencing factors and causes of different types of landslides, and investigate the distribution characteristics of potential landslides. A total of 609 historic landslides have been interpreted in the study area and were found to be distributed along faults and locally concentrated. The strata from which landslides develop are relatively weak and are mainly distributed within 2 km of a fault with a slope between 20° and 30°. The direction of slope for the majority of landslides is south to south-west, and their elevation is between 4000 and 5000 m. In addition, we discovered a power law relationship between landslide area and volume ($V_L = 2.722 \times A_L^{1.134}$) and determined that there were 47 super-large landslides, 213 large landslides, and 349 small and medium-sized landslides in the area, respectively. Slope is the most significant influencing factor for the development of landslides in the area. Apart from slope, faults and strata significantly influence the development of large and medium-small landslides, respectively. We have identified 223 potential landslides in the region, 15 of which directly threaten major transport routes, mainly in the Renbu Gorge section of the China–Nepal Highway and the proposed China–Nepal Railway section from Peikucuo to Gyirong County. In addition, we also discussed the causes of landslides within three geomorphic units in the region. First, the combined effects of faulting, elevation, and relatively weak strata contribute to the development of super-large and large landslides in the Gyirong basin and gorge. Second, the relatively weak strata and the cumulative damaging effects of earthquakes promote the development of small and medium-sized landslides in the Xainza-Dinggye rift basin. Third, under the combined effect of the hanging wall effect of thrust faults and the relatively weak material composition, landslides of various types have developed in the Nagarzê mountain. It is worth noting that potential landslides have developed in all three geomorphic units mentioned above. This study provides data and theory to assist in the accurate mitigation and control of landslide hazards in the corridor.

Keywords: the China–Nepal transportation corridor; remote sensing; landslides; the influencing factors of landslides; machine learning; ITPA technology

check for updates

Citation: Zhao, S.; Zeng, R.; Zhang, Z.; Meng, X.; Qi, T.; Long, Z.; Guo, W.; Si, G. Landslide Mapping and Causes of Landslides in the China–Nepal Transportation Corridor Based on Remote Sensing Technology. *Remote Sens.* **2024**, *16*, 356. https://doi.org/10.3390/rs16020356

Academic Editor: Sandro Moretti

Received: 28 November 2023
Revised: 7 January 2024
Accepted: 12 January 2024
Published: 16 January 2024

Copyright: © 2024 by the authors. Licensee MDPI, Basel, Switzerland. This article is an open access article distributed under the terms and conditions of the Creative Commons Attribution (CC BY) license (https://creativecommons.org/licenses/by/4.0/).

1. Introduction

China has one of the worst landslide records in the world [1]; 126,000 landslides occurred in China from 2009 to 2018, resulting in 6280 casualties and direct economic losses of approximately 43.7 billion yuan (Ministry of Natural Resources, People's Republic of China). Rainfall, freeze-thaw cycles, river erosion, and human engineering activities are external dynamic factors that can trigger landslides [2–5]. Active faults, regional tectonic deformation, changes in the crustal stress field, and earthquakes are internal dynamic factors [6,7]. Compared with landslides induced by single factors such as earthquakes and rainfall, the coupling effect of internal and external dynamics is more likely to breed catastrophic super-large and large landslides [8,9]. The Qinghai–Tibet Plateau is currently one of the regions with the most intense neotectonic activity and climate change sensitivity worldwide. There are three causes of landslides, taking the southern Qinghai–Tibet Plateau as an example. (1) Tectonic effect: Faults can destroy the structure and integrity of the slope rock mass, reduce its mechanical strength, and control the slope failure mode [10]. Thrust faults can have a hanging wall effect and are frequently associated with the development of numerous landslides [11]. (2) The impact of earthquakes: On the one hand, densely distributed suture zones and active faults may trigger seismic events, triggering large-scale landslides [12]. On the other hand, strong earthquakes lead to the formation of joints and fissures within slopes, and the infiltration of water (precipitation, ice, and snow melt) leads to the reduction of rock and soil strength and the expansion of cracks, significantly reducing slope stability [8,13]. (3) Non-triggering factors: Some large landslides are caused by the cumulative effects of multiple adverse geological environmental factors rather than a single factor. Strong crustal uplift and river incision lead to valley deepening. Under the influence of unloading and rebounding of the rock mass, the violent stress release of the slope rock mass in the high-stress zone provides the energy for the formation of deep deformation and fractures [9,14,15]. In addition, over a long geological history, the slope rock mass has collapsed and buckled under the weight of its own mass and glaciers. Long-term freeze-thaw cycles progressively weaken the shear strength of the rock mass and structural surfaces. As a result of precipitation and the melting of glacial snow, the structural surfaces of the rock and soil became softer, and the pore water pressure increased, leading to slope instability [16–18].

The China–Nepal Transport Corridor is a road for economic development and is vital to the country's efforts to build a land trade route in South Asia and promote the Ring-Himalayan Economic Cooperation Belt. It consists of the China–Nepal Highway (an existing road) and the China–Nepal Railway (a planned railway). The China–Nepal Highway starts in Lhasa and ends in Kathmandu, the capital of Nepal. The 829 km Chinese section passes through Qushui County, Shigatse City, Lazi County, Tingri County, and Zhangmu town, ending at the Friendship Bridge. The 540 km Chinese section of the China–Nepal Railway starts from Shigatse City in the east, passes through Saga County, Tingri County, and Gyirong County, and ends at Gyirong Port (Figure 1b). The study area is located in the southern portion of the Qinghai–Tibet Plateau, passing from north to south through three secondary tectonic units: the Lhasa Block, the Himalayan Blocks, and the YarlungZangbo River suture zone [19]. Strong compression of nearly north-south tectonic stress causes the boundary faults of tectonic units at all levels to predominantly strike east-west [20]. These faults are generally characterized by a long extension distance, large cutting depth, fault fracture bandwidth, and multistage activity [21]. Moreover, river downcutting and freeze-thaw erosion are intense [22]. Therefore, disastrous landslides are possible in the region due to the coupling of internal and external dynamics [23], which threatens the safe operation of the China–Nepal highway and the construction of the China–Nepal railway. Due to the fragile geological environment of the China–Nepal transport corridor, climate warming may contribute to an increase in the frequency and probability of landslide disasters in the study area, manifested in the resurgence of old landslides and the induction of potential landslides. At present, scholars are concentrated on the structural characteristics, deformation monitoring, and stability assessment of specific landslides along the China–Nepal transportation corridor [24–26]. In addition, research on the interpretation, development characteristics, and driver factors for historical landslides in the local areas has been conducted using a single remote sensing interpretation or field survey method [27–29]. However, there is a lack of systematic research on the distribution and causes of landslides (old landslides and potential landslides) in the study area. Therefore, it is a challenge to provide scientific prevention before and rapid emergency response after landslides along the China–Nepal transportation corridor.

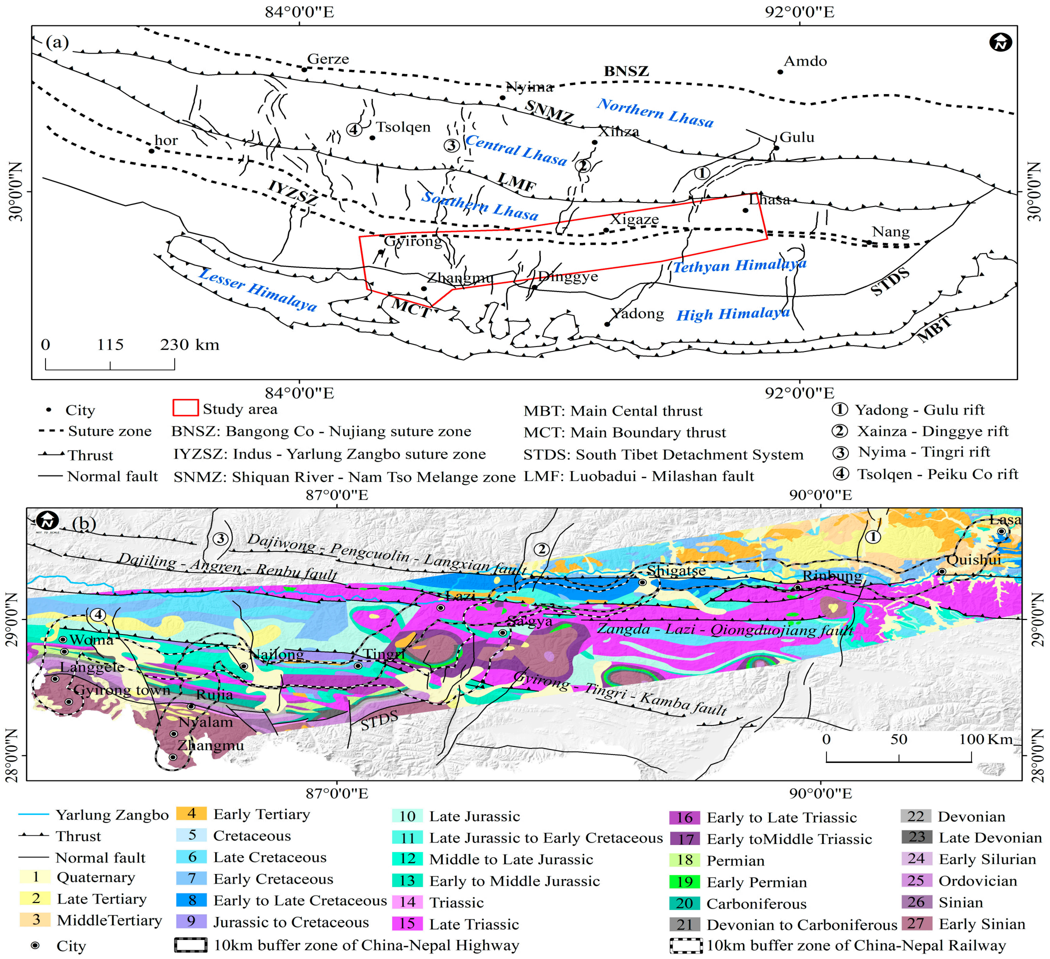

Figure 1. Overview of the study area. (**a**) Geographical location and geotectonics [30]; (**b**) geological maps and the distribution of major faults.

Considering the above context, we are conducting research on landslide cataloging, spatial distribution patterns, controlling factors, causes of landslides, and potential landslide hazard threat areas along the China–Nepal transport corridor using remote sensing, field survey, and mathematical statistical analysis methods. This will fill a gap in the current research on landslides along the whole line of the China–Nepal transport corridor. This work will also benefit the precise prevention and control of landslide disasters along the China–Nepal Highway and the construction of the China–Nepal Railway.

2. Overview of the Study Area

2.1. Tectonic Activity

The collision of the Indian and Eurasian plates resulted in the uplift of the Qinghai–Tibet Plateau [31]. The Bangong Co-Nujiang Suture Zone (BNSZ), Indus-Yarlung Zangbo Suture Zone (IYZSZ), and Main Boundary Thrust (MBT) divide the southern Qinghai–Tibet Plateau into two blocks, the Lhasa and Himalaya blocks [30,32]. The China–Nepal transport corridor includes four blocks from north to south: the South Lhasa Block, the Tethys

Himalaya, the High Himalaya, and the Lower Himalaya (LT) [19,30,32,33] (Figure 1a). Late in the Miocene, the Qinghai–Tibet Plateau began to extend towards the east-west, and the north-south rift (normal fault) formed. This was the most significant tectonic event in southern Tibet and the northern Himalayas [19,34,35]. The better-known are the Yadong-Gulu, Nyima-Tingri, Xainza-Dinggye, and Tsolqen-Peiku Co rifts [34,36], with the first three rifts extending at rates of 4–5 mm/yr, 4–5 mm/yr, and 1–2 mm/yr, respectively [37]. Since the Quaternary, these rifts have been the most notable active structures in the study area [38], as well as the center area of late Cenozoic magmatic activity and the development area of shallow earthquakes today [39,40]. In addition, the approximately east-west trending Dajiwong-Pengcuolin-Langxian fault, Dajiling-Angren-Renbu fault, Zangda-Lazi-Qiongduojiang fault, and Gyirong-Tingri-Kangba faults intersect with the north-south fault, forming a grid of faults throughout the region (Figure 1b). In conclusion, tectonic activity has created a complex and fragile geological environment in the region, and intense neotectonic activity is likely to create geological structural conditions that are conducive to landslides.

2.2. Lithology

The strata in the study area are complex and diverse (Figure 1b). Langgele Village to Gyirong Town and Rujia Village to Zhangmu Town are part of the High Himalayan Block, which consists of high-grade metamorphic rocks from the Paleoproterozoic to the Ordovician, including hornblende-phase gneisses, calcic siliceous rock and marble, and some areas containing light-colored granites [32,41]. The Lhasa to Qushui Section is located to the north of the Yarlung Zangbo River and is a part of the South Lhasa Block, with exposed granite, Jurassic to Cretaceous sedimentary rocks, and Quaternary alluvial deposits [42,43]. The region south of the Yarlung Zangbo River up to Rujia and Langgele Village is a part of the Tethys Himalayan Block, a marine sedimentary stratum with relatively soft lithology. The main strata consist of Paleozoic to Cenozoic shallow metamorphic clastic rocks and carbonate rocks, with lithology including quartz sandstone, miscellaneous sandstones, mud shale, and greywacke [44] and rocks formed through intermediate-low grade metamorphism, such as slate, phyllite, and marble [36,45]. In summary, there may be lithological conditions in the region that are conducive to the formation of landslides.

2.3. Topographic and Climatic Characteristics

Previous studies have shown that more precipitation will increase the frequency of landslid activities in areas of high elevation and undulating topography, thereby increasing the risk of slope geological hazards [22]. Strong crustal uplift, tectonic rifting, weathering denudation, and water erosion have produced an alternate geomorphic pattern of alpine canyons and intermountain basins in the region, with the topography being high in the west and low in the east, with an elevation difference of 5174 m. The climatic conditions in the region exhibit substantial spatial variation. A subtropical monsoon climate prevails in the regions of Langgele Village in Gyirong County and Rujia Village in Nyalam County, which are influenced by the Himalayas. The average annual rainfall ranges from 1000 to 2820.6 mm, and over 80% of the annual precipitation falls from June to September [46]. The other regions have a temperate semi-arid plateau monsoon climate with annual average precipitation between 265.3 and 451.5 mm, with 70% of the annual precipitation falling between June and September. Therefore, there may be topographical and climatic conditions in the region that are conducive to landslide development.

3. Data and Methodology

3.1. Data Sources

This research makes use of optical remote sensing imagery, radar imagery, stratigraphic data, and fault data. For historical landslid interpretation, optical remote sensing imagery with a resolution of 0.50 m from the Google Earth platform was used. C-band imagery of

Sentinel-1A (5 m range resolution and 20 m azimuth resolution) was used to determine the ground deformation. All data were collected from ascending orbits along tracks 41, 114, 12, and 85 and covered a total of 111 images between January and December 2021. The data coverage is depicted in Figure 2.

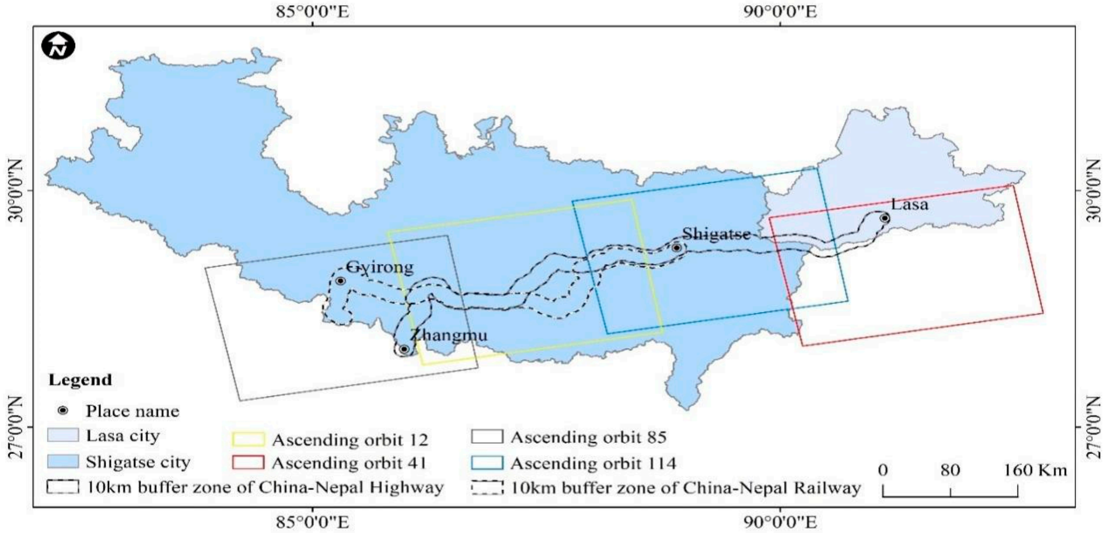

Figure 2. Coverage of data from Sentinel-1A in the study area.

The China Earthquake Administration provided the seismic data used to analyze landslide control factors, whereas the China Geological Survey provided the 1:500,000 geological map and tectonic maps. The United States Geological Survey provided the ASTER GDEM with a 30 m resolution, which was used for topographic phase removal and geocoding during InSAR processing.

3.2. Historical Landslide Mapping

The cumulative effects of numerous landslip events over decades, centuries, or millennia are revealed by geomorphic historical landslide inventories [47]. The automatic recognition of landslides is based on high-quality landslide data represented by polygon features. It is necessary to divide the landslide data into a training set and a test set [48]. Then, machine learning methods such as logistic regression, support vector machines, random forests, deep learning, and convolutional neural networks are used to test whether the landslides in the inventory can be correctly classified, and finally, the effectiveness of different models is evaluated. However, the study area lacks a landslide database, making it difficult to directly conduct automatic landslide recognition. The literature research is a reliable method for landslide mapping. The literature review is a reliable method for landslide mapping. However, within a specific region, the landslide data recorded in the literature may be limited or missing [49]. The field survey method has a high degree of reliability. The optical remote sensing imagery from the Google Earth platform has a three-dimensional effect that helps in the recognition and interpretation of landslides [50,51], but the method is subjective. All of the aforementioned methods can be used to map historical landslides, but the use of a particular interpretation method alone will increase the likelihood of landslide misses and misclassifications. It is challenging to conduct a large-scale field survey along the China–Nepal transport corridor due to the terrain's high altitude, complexity, and diversity. Therefore, we combine the three for landslide mapping. First, we saved the landslides whose latitude and longitude were documented in the literature for a preliminary inventory of landslides in the study area. For the landslide data recorded as images in the literature, they were registered and digitized in ArcGIS by place name, longitude, and latitude, and then stored. Second, the historical landslides were interpreted based on optical image textures, feature markers (Google Earth platform), and topographic data. Next, a four-person field survey was conducted to verify the preliminary landslide inventory, which consisted of a literature review and visual interpretation (accessible areas along the road). Finally, misinterpreted landslides were removed and missing landslides were added, resulting in the final landslide database.

The following are the interpreted characteristics of landslides in the region: (1) There is a substantial tonal distinction between the landslide mass and the surrounding environment and a distinct boundary (Figure 3a). (2) The tone of the landslide mass matches the surrounding environment, but the backwalls, the sidewalls, and the tongue of the landslide are obvious. The sliding source area is recessed, with steep backwalls and bright colors. In addition, the material of a landslide is fragmented and coarse (Figure 3b). (3) After a lengthy period of internal and external force modification, the landslip body has the same color as the surrounding terrain, and a slope gully has formed (Figure 3c).

Figure 3. Characteristic features used for interpretation of historical landslides. (**a**) New landslide; (**b**) Old landslip with a visible rear wall and slip source; (**c**) Old landslides that have formed gullies.

3.3. Landslide Volume Calculation

Due to the complexity of the environmental conditions for a landslide and the uncertainty of the depth of the sliding surface, estimating the volume of landslides on a regional scale is a difficult task [52]. Nevertheless, the mathematical relationship between landslide area and volume is essentially independent of the natural environment [53], i.e., ignoring the properties of the landslip itself, such as its depth and shape. Consequently, mathematical statistical analysis based on landslide area (A_L) and volume (V_L) is currently regarded as a mature empirical method for estimating landslide volume at present [53–55]. The following is the formula:

$$V_L = \varepsilon \times A_L^{\alpha} \tag{1}$$

V_L is the volume of the landslide, A_L is the area of the landslide, and ε and α are fitting parameters.

3.4. Interferometric Synthetic Aperture Radar (InSAR) Technology

InSAR technology has been used for landslide detection and deformation monitoring [56,57]. The basic idea of Interferometric Point Target Analysis (IPTA) is to use multiple SAR images covering the study area to perform time series analysis. The differential phase of each point target is then separated to obtain surface deformation information for the corresponding time period in the study area. The specific processing steps are as follows: Firstly, import the acquired SAR data into the GAMMA software (v20210701). An image with small temporal and spatial baselines is selected as the master image, and the other images are registered to this master image. The registered images are then clipped. Secondly, interferometric pairs are generated with a time baseline of 25 days, and differential interferograms are produced using the two-pass differential method. Each differential interferogram contains a deformation phase, a DEM error phase, an atmospheric phase, and a noise phase [58]. Thirdly, Permanent Scatterers (PS) points are selected using spectral diversity analysis and the amplitude dispersion index [58,59]. Vector data format single-pixel (PSI) differential interferometric phases are generated for the selected

PS points. Subsequently, reference points are selected in a relatively stable area at the center of the study region. The minimum cost flow method is applied for phase unwrapping. A two-dimensional regression analysis method is used for iterative calculations of the interferometric phase in the time dimension. The phase differences between the remaining target points and the reference points are analyzed to obtain the linear deformation velocity of the study area, DEM error correction values, and residual phase (which includes atmospheric and noise phases) [58]. Finally, spatiotemporal filtering is used to separate the atmospheric phase, noise phase, and nonlinear deformation phase from the residual phase. The linear and nonlinear deformation phases are combined, and the Singular Value Decomposition (SVD) method is used to extract the time-series deformation information.

3.5. Correlation between Landslides and Influencing Factors

Feature selection is a critical step in data analysis and machine learning, as it helps us select the most representative and relevant features from a large set of attributes. The Pearson correlation coefficient is a statistical index used to measure the linear relationship between two continuous variables, with values ranging from -1 to 1. A value of -1 indicates a negative correlation, +1 indicates a positive correlation, and 0 indicates no linear correlation. The chi-square test can be used to examine whether there is an association between two categorical variables. A higher chi-squared value indicates a stronger association between the feature and the target variable, indicating greater importance, with values ranging from 0 to positive infinity. Before calculating the correlation coefficients and performing the chi-square test, the obtained data for faults, strata, slope, aspect, elevation, precipitation, and temperature were resampled to a resolution of 30 m $\times$ 30 m to ensure that all factors had the same pixel size. Each factor was then normalized. Landslides that have already occurred are marked as 1, while an equal number of randomly selected non-landslide points within the study area are marked as 0. Next, the normalized factors are assigned to both landslide and non-landslide points. The relationship between landslides and influencing factors is assessed quantitatively using the Pearsonr function from the Scipy library and the Chi2 function from the Sklearn library in Python.

4. Results

4.1. Landslide Area–Volume

Due to the age of the landslides within the area, there is no Digital Elevation Model (DEM) available from before the landslides occurred, making it impossible for us to accurately calculate the volume of landslides along the China–Nepal transportation corridor. On the other hand, among the existing studies in the region, only 14 landslides have both area and volume information, making the empirical formula for the area-volume relationship of landslides based on this data one-sided. Here, through a literature survey, we collected 89 landslides (the landslide areas are between 6×10^2 m^2 and 2.25×10^7 m^2, and the landslide volumes were between 6×10^3 m^3 and 3.5×10^9 m^3) of known area and volume in southern Tibet (the China–Nepal Transportation Corridor is part of it) (Figure 4a) in order to establish a power-law relationship between landslide area and volumes (Equation (2)). There is a distinct linear relationship between the logarithms of landslide area and volume, as shown in Figure 4b. The line of best fit (solid red line) on the binary kernel density map passes through the maximum density region (the landslide area is 1×10^5 m^2 < A_L < 1×10^5 m^2, and the landslide volume is 1×10^5 m^3 < V_L < 1×10^5 m^3). Only two of the landslides were outside the 95% predicted interval (red dotted line), while 98% were in close proximity to the fitted line.

$$V_L = 2.722 \times A_L^{1.134} \tag{2}$$

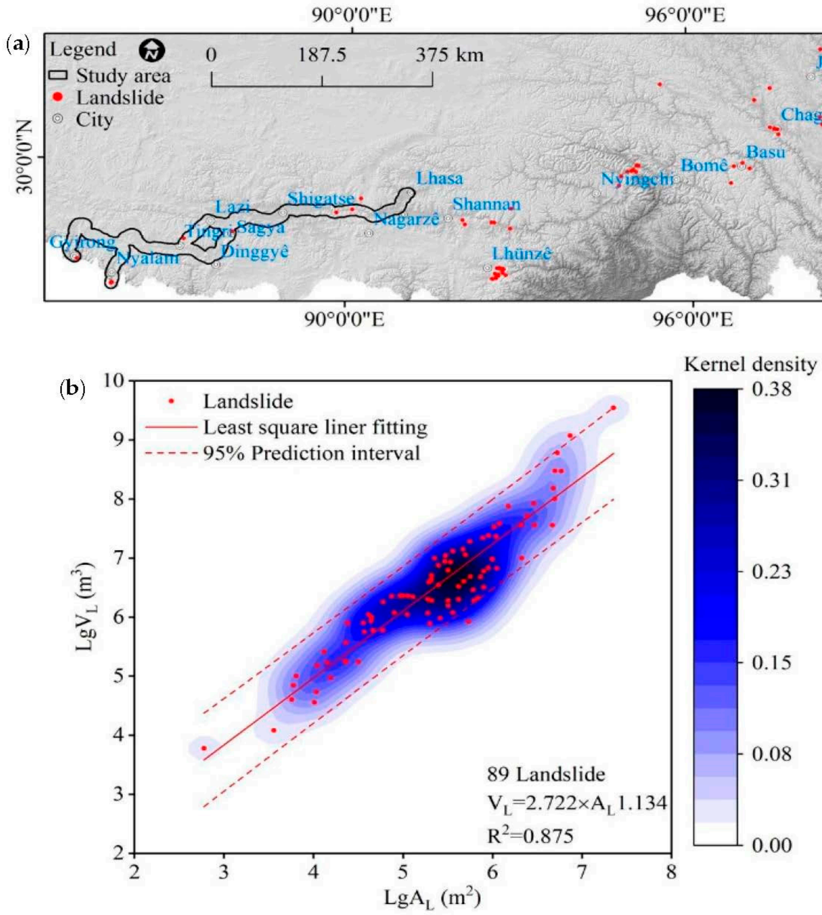

Figure 4. (**a**) Landslide in southern Tibet. (**b**) The logarithmic power-law relationship between the area and volume of landslides. The solid red line represents the line of best fit, whereas the dashed red line represents the 95% prediction interval.

4.2. Interpretation of Historical Landslides

Due to the lack of available optical remote sensing images and documentation in the area, it was impossible to determine when the landslide took place. Therefore, only spatial information on landslides was cataloged. A total of 609 historical landslides with areas ranging from 6.13×10^2 m^2 to 2.46×10^6 m^2 were mapped using the interpretation of remote sensing data and field surveys, of which 293 landslides have been verified in the field (Figure 5). Their volume ranged between 1.6×10^3 m^3 and 4.8×10^7 m^3 (Equation (2)), with 47 super-large (volume larger than 10 million cubic meters), 213 large (volume between 1 million and 10 million cubic meters), and 349 small and medium-sized landslides (volume less than 1 million cubic meters). The super-large and large landslides account for 42.7% of the total number of historical landslides.

The spatial distribution of landslides in the region exhibits the following characteristics: First, the majority of super-large and large landslides are primarily distributed along faults and ridges (Figure 5b,c) and are mainly spatially distributed in the Gyirong basin and Gorge, the Yalai-Menbu Mountain in Nyalam County, the Nagarzê Mountains in Shannan City, and the Lazi-Tingri Mountain. The small and medium-sized landslides mainly develop along gullies and are distributed in the Xainza-Dinggye Rift Basin and Zhangmu Valley. Second, historical landslides exhibited a dispersed and locally localized distribution and mainly occurred in the Gyirong basin and gorge (Figure 5e), the Xainza-Dinggye Rift Basin, the Nagarzê mountains in Shannan City, and the Lazi-Tingri Mountain (Figure 5d).

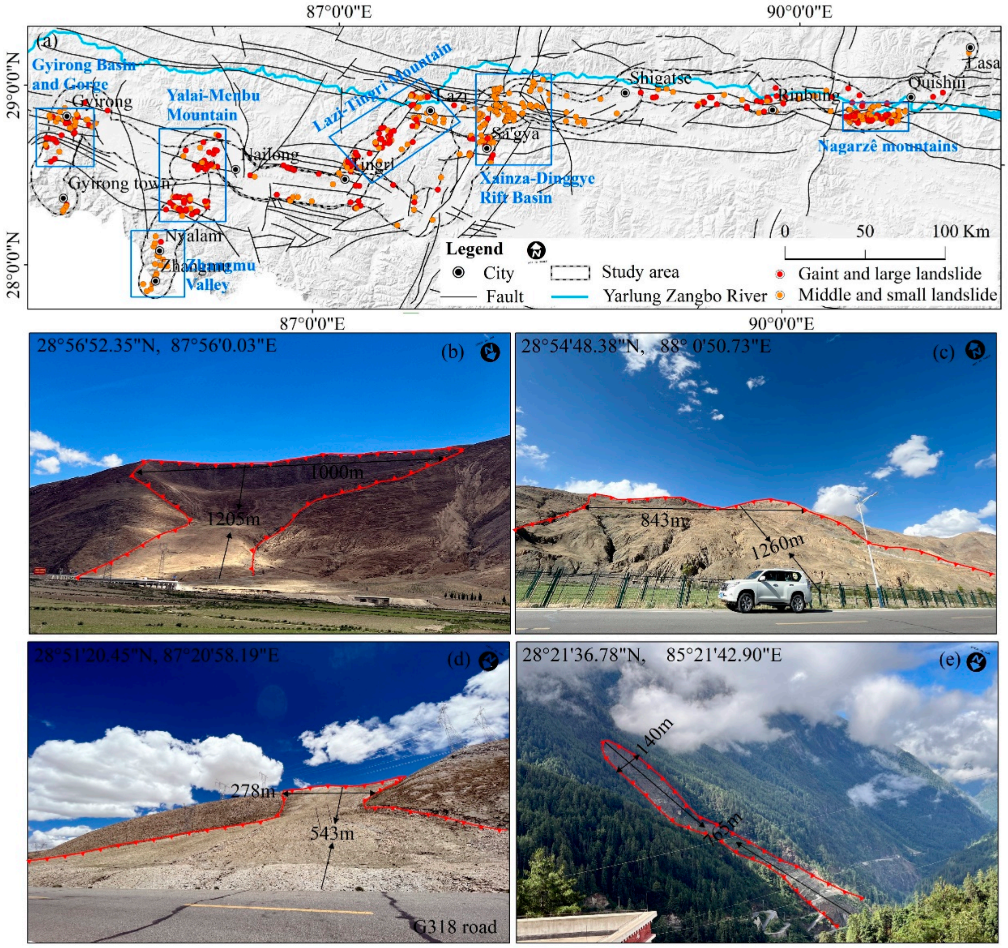

Figure 5. Spatial distribution of landslides and typical the China–Nepal transport corridor. (**a**) Spatial distribution of historical landslides; (**b**,**c**) landslides in the Xainza-Dinggye Rift Basin and on National Highway G219; (**d**) landslides in the Lazi-Tingri Mountain and on National Highway G318; (**e**) landslides in the Gyirong and on National Highway G219.

4.3. Factors That Influence Landslides

The formation of landslides is a complex process influenced by various factors, such as topography, lithology, structure, erosion, and climate. In this work, we chose factors for classification statistics that may have large differential effects on individual landslides at the regional scale, including altitude, slope, aspect, stratum, distance from faults, precipitation, and temperature. It should be noted that the average value of each landslide's surface data are used in the extraction of factors.

Faults. Faults influence the structural integrity of slope rock masses, the variability of the regional tectonic stress field, and the distribution of landslides [60,61]. Mathematical statistical analysis shows that the number of landslides is negatively connected with the distance from a fault (Figure 6a), which is related to the gradual decrease in fault-driven damage to the rock mass with increasing distance from the fault [62]. We calculated the number of landslides at various distances from faults, and the results suggest that the majority of landslides (57.80%) occur within 2 km of a fault, and the number of landslides decreases significantly beyond 2 km (Figure 6a). Previous research has revealed that tectonic activity has an essential role in the formation and development of large landslides [63], which frequently occur along fault zones [61,64]. As can be seen from Figure 7a, the distribution of super-large landslides within 1 km of a fault accounts for 48.94% of all super-large landslides. The proportion of super-large, large, small, and medium-sized landslides occurring within 2 km of a fault was 61.70%, 59.15%, and 56.45%, respectively. The number of super-large and large landslides falls fast at distances greater than 2 km; however, the tendency is less obvious for small and medium-sized landslides. Therefore, while other plausible causes of small and medium-sized landslides cannot be ruled out in this study, it is sufficient to demonstrate the control effect of tectonic activity on regional landslides.

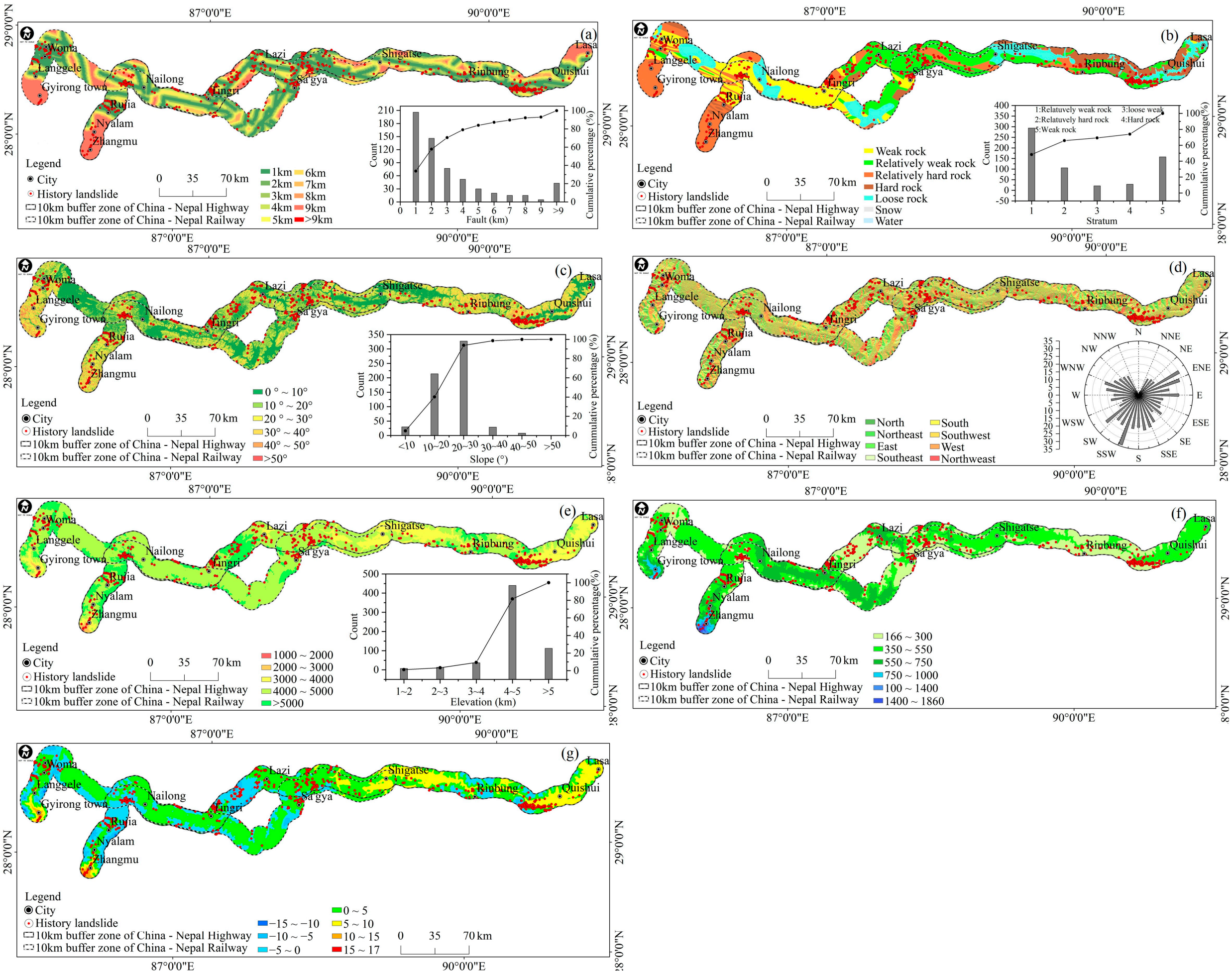

Figure 6. Spatial relationships between historical landslides and influencing factors: (**a**) fault; (**b**) lithology; (**c**) slope; (**d**) aspect of slope; (**e**) altitude; (**f**) precipitation; and (**g**) temperature.

Lithology. Lithological sequences reflect the physical and mechanical properties of geological structures that cover an area's surface [65], influencing the weathering degree of the slope material and the strength and permeability of the rock mass [66]. Relatively weak strata are more vulnerable to external erosion [67], which is conducive to landslide development. The region's relatively soft rocks are mainly shale, limestone, marlstone, metamorphic sandstone, siltstone, sandy mudstone, mudstone, slate, and phyllite from the Late Triassic Xiukang, the Early to Middle Jurassic Ridang, and the Early to Late Cretaceous Shigatse groups, with some rocks having an interbedded structure [68,69]. Our statistical findings demonstrate that the majority of landslides are distributed in weak and relatively weak strata, accounting for 74.22% of all landslides (Figure 6b). Furthermore, in weak and relatively weak strata, roughly 65.96% of landslides were super-large, 78.87% were large-scale, and 72.78% were small and medium-sized (Figure 7b). Furthermore, 22.17% of landslides are distributed in hard and relatively hard strata (mostly the Pre-Sinian Quxiang Group gneiss, schist, and granulated sandstone), with super-large, large, small, and medium-sized landslides accounting for 25.53%, 18.31, and 24.07%, respectively. It is worth noting that earthquakes in Nepal may contribute to landslides in relatively hard strata, which are primarily concentrated in the towns of Zhangmu and Gyirong. According to the statistical results of landslide distribution in strata, the properties of the strata in the area have a positive impact on landslide distribution. Specifically, weak and relatively weak strata may be the most important stratigraphic conditions for the development of landslides.

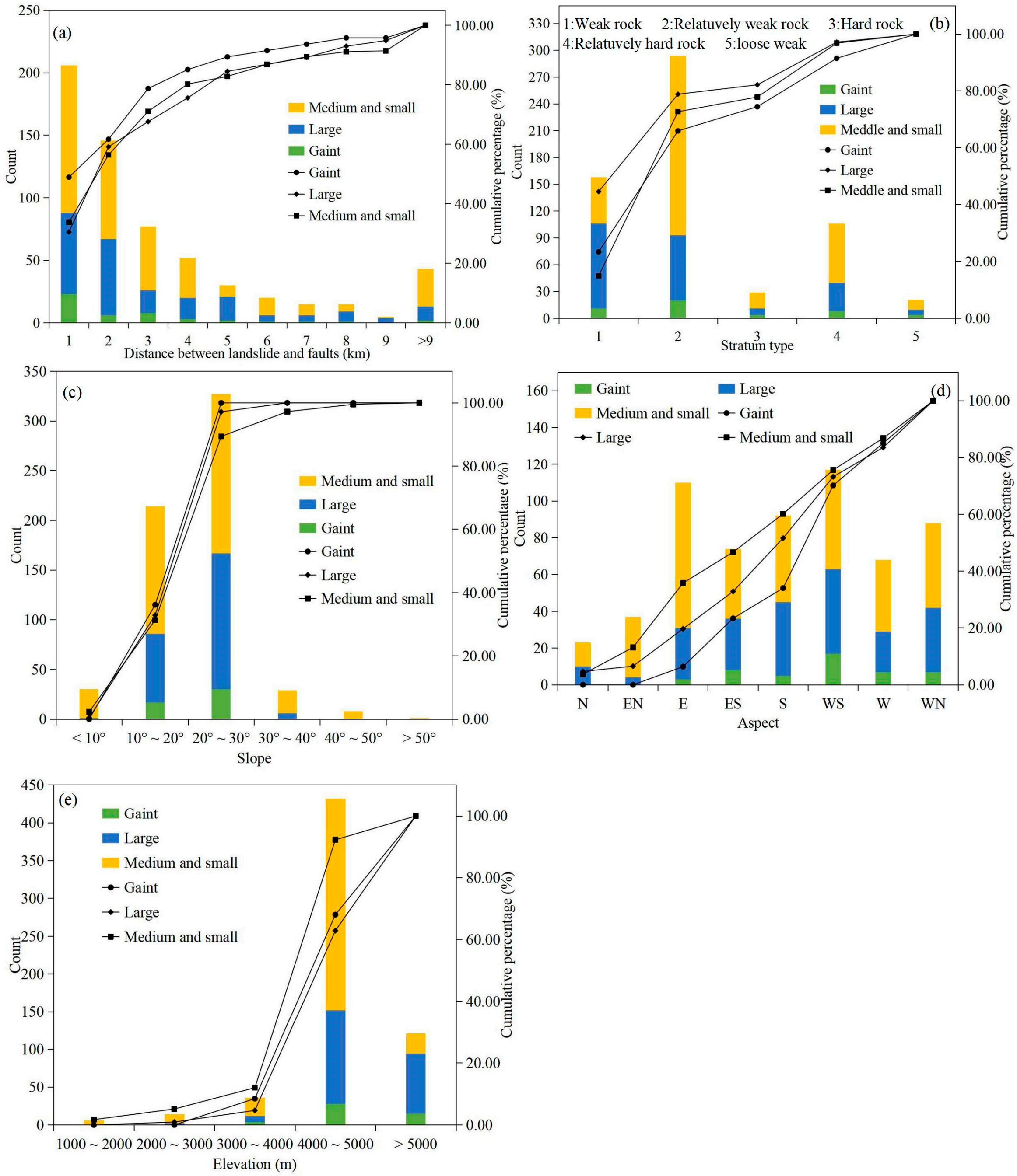

Figure 7. Relationships between landslides of different scales and different influencing factors: (**a**) faults; (**b**) lithology; (**c**) slope angle; (**d**) slope aspect; (**e**) altitude.

Slope. The slope gradient controls a slope's shear stress [66]. The faster the slope gradient exceeds the slope stability limit, the greater the possibility of a landslide [70]. Our statistical results indicate that as the slope gradient increases, the number of landslides in the area increases and then decreases in a normal distribution. In addition, the terrain slopes where landslides occur in this region are generally concentrated between 10° and 30°, with a total of 541 landslides, accounting for 88.83% of the total number of landslides in the region. The slope of 20–30° is the interval with the highest frequency of landslide development, accounting for 53.69% of all landslides (Figure 6c). The intervals with slopes less than 10° and greater than 30° have fewer landslides, accounting for 4.93% and 6.24%, respectively. Notably, our statistical results also indicate that super-large and large landslides are all concentrated on slopes between 10° and 30° (Figure 7c), which is evidently distinct from small and medium-sized landslides.

Slope aspect. The slope aspect influences the duration of sunshine. When the slope is exposed to protracted sunlight, the rock and soil mass may contract and expand to a greater degree, resulting in a high degree of damage to the rock mass and a reduction in slope stability [71]. The slope aspect influences soil moisture and vegetation distribution, which in turn impacts landslide evolution processes [72]. Approximately 34.32 percent of the region's landslides are concentrated on the sunny slope (157.5°–247.5°, or east-to-southwest direction) (Figure 6d). As the landslide scale increases, the slope aspect distribution of landslides becomes more concentrated. For example, in the direction of the sunny slope, the number of super-large landslides (46.81%) > large landslides (37.09%) > small and medium-sized landslides (26.93%) (Figure 7d).

Altitude. The intensity of erosion is related to altitude. Our statistical analysis indicates that as altitude increases, the frequency of landslides increases rapidly and then decreases. They are mainly concentrated in the extremely high mountains, with large fluctuations caused by denudation, erosion, and periglacial processes in the altitude range of 4000 m to 5000 m (Figure 6e), accounting for 80.13% of the total number of landslides, among which the proportions of super-large, large, small, and medium-size landslides were 91.49%, 95.31%, and 87.97%, respectively (Figure 7e). Due to the higher altitude of the Qinghai–Tibet Plateau and the distribution of most faults along the ridges, the geological structure is more fragmented here [60]. In addition, strong physical weathering occurs in regions at high altitudes. Numerous landslides have occurred in the region as a result of the aforementioned causes. Compared to super-large and large landslides at altitudes below 4000 m, small and medium-sized slides are the most common and are concentrated along highways and secondary valleys.

Temperature and precipitation are the two most important factors contributing to landslide occurrence in high-altitude regions [3]. Annual precipitation generally affects landslide development in two ways. On the one hand, rainfall infiltration increases the moisture content of the slope, which gradually reduces its shear strength, thus providing essential conditions for landslide occurrence. On the other hand, precipitation directly leads to the deterioration of slope structure, which subsequently leads to landslides [73]. Therefore, on a regional scale, precipitation is generally considered an indispensable external factor for landslide development [74]. In high-altitude mountainous areas, temperature plays a critical role in the occurrence of landslides. Research has shown that rising temperatures lead to the melting of snow or ground ice, which in turn causes permafrost degradation and increases dynamic water pressure at the base of the active layer, thereby triggering or exacerbating mountain landslides [3,75]. Due to the presence of a subtropical monsoon climate and a temperate semi-arid plateau climate in the area, there are significant spatial differences in precipitation and temperature. The maximum difference in annual precipitation can reach 1694 mm (Figure 6f), and the maximum difference in temperature can reach 32 °C (Figure 6g). However, the influence of rainfall and temperature on landslides in this region needs to be clarified. Therefore, we only calculate the correlation between landslides, precipitation, and temperature quantitatively at the regional scale.

In short, landslides in the region are distributed along faults and mainly develop in weak and relatively weak strata within 2 km of faults, on slope angles between 20° and 30°, with south to southwest slope aspects, and at elevations between 4000 and 5000 m.

In addition, we have quantitatively calculated the correlation coefficient between landslides and influencing factors using the Pearson chi-square test and the Pearson correlation coefficient. The calculation results show that the slope has the highest score and correlation (Figure 8a,b), making it the most significant factor in the development of landslides along the China–Nepal transportation corridor. This is followed by stratigraphy and faults, which are consistent with the results of our previous statistical analyses. In addition, we found that there are differences in the controlling factors for landslides of different scales within the study area. In addition to slope, faulting, temperature, and elevation have higher scores for large and super-large landslides (Figure 8c,d). Moreover, the scores for these factors are similar. This also suggests that the coupled effects of multiple factors are conducive to the development of very large and super-large landslides. In addition to slope, the stratum significantly influences the development of medium and small landslides, followed by altitude and precipitation (Figure 8e,f).

4.4. Landslide Potential Threat Area

Based on 111 scenes of Sentinel-1A data, we used ITPA technology to calculate that the annual ground deformation velocity in the China–Nepal transportation corridor is about −320 mm–364 mm (Figure 9a), and the annual surface deformation velocity for the segments from Gyirong and Zhangmu to Dingri (Figure 9b), Tingri to Shigatse (Figure 9c), and Shigatse to Lhasa (Figure 9d) are −320 mm–364 mm, −272 mm–145 mm, and −295 mm–364 mm, respectively. We set a relative stability threshold based on the standard deviation and average value of the deformation points. Areas with an annual deformation rate between −15 mm and 15 mm are categorized as relatively stable zones, while areas exceeding this range are identified as deformation zones. Using this threshold, a total of 705 deformation zones were initially identified. We superimposed the boundaries of these deformation areas on the Google Earth optical remote sensing image and used this, combined with field survey and verification, to further classify surface deformation into three types based on the distribution of deformation zones and their corresponding characteristics: potential landslides, glacier movements, and slope weathering layers.

Potential landslides in the area include the local revival of old landslides and new potential landslides. The main characteristics of the local revival of an old landslide are a large number of cracks and scarps on the original fractured landslide mass, the occurrence of slides and collapses, and a bright back wall of the landslide (Figure 10b,d). The main characteristics of a new potential landslide are the fractured rock and soil mass of the slope surface, the steep scarp at the back edge of the slope, the tension crack at the front edge, and the subsidence in the middle of the slope. In addition, gullies have developed on the slope surface, and loose material has gathered in the valley (Figure 10c). Glacier movements are mainly distributed south of Gyirong Town and Nielamu County (in the subtropical monsoon climate zone) within U-shaped troughs at altitudes above 5000 m. The maximum annual surface deformation rate can reach 300 mm. The primary morphology is characterized by striations and tongues with clear boundaries (Figure 10e,f), making them easily distinguishable. Slope weathering layers are distributed across the mountaintops throughout the region. Mainly distributed in periglacial landforms and eroded and denuded extremely undulating alpine landforms. The tops of these slopes are subject to intense solar radiation and significant diurnal temperature variations. After weathering, the rock and soil layers on the slope's surface experience surface slip, resulting in distinct color differences and rough textures in the images compared to the surrounding features.

According to the above interpretation signs, 233 potential landslides were identified in the study area, 36 of which were local revivals of old landslides and 187 of which were new potential landslides. The spatial distributions of potential and historical landslides are consistent (Figure 5), and they are geomorphologically concentrated in the Gyirong basin and gorge, the Lazi-Tingri Mountain, Nagarzê Mountain in Shannan City, and the Xainza-Dinggye Rift Basin. There are fifteen potential landslides that pose a direct threat to traffic arteries, primarily in the Renbu Canyon section of the China–Nepal Highway and on both sides of the proposed China–Nepal Railway (Pekucuo to Gyirong County section) (Figure 11).

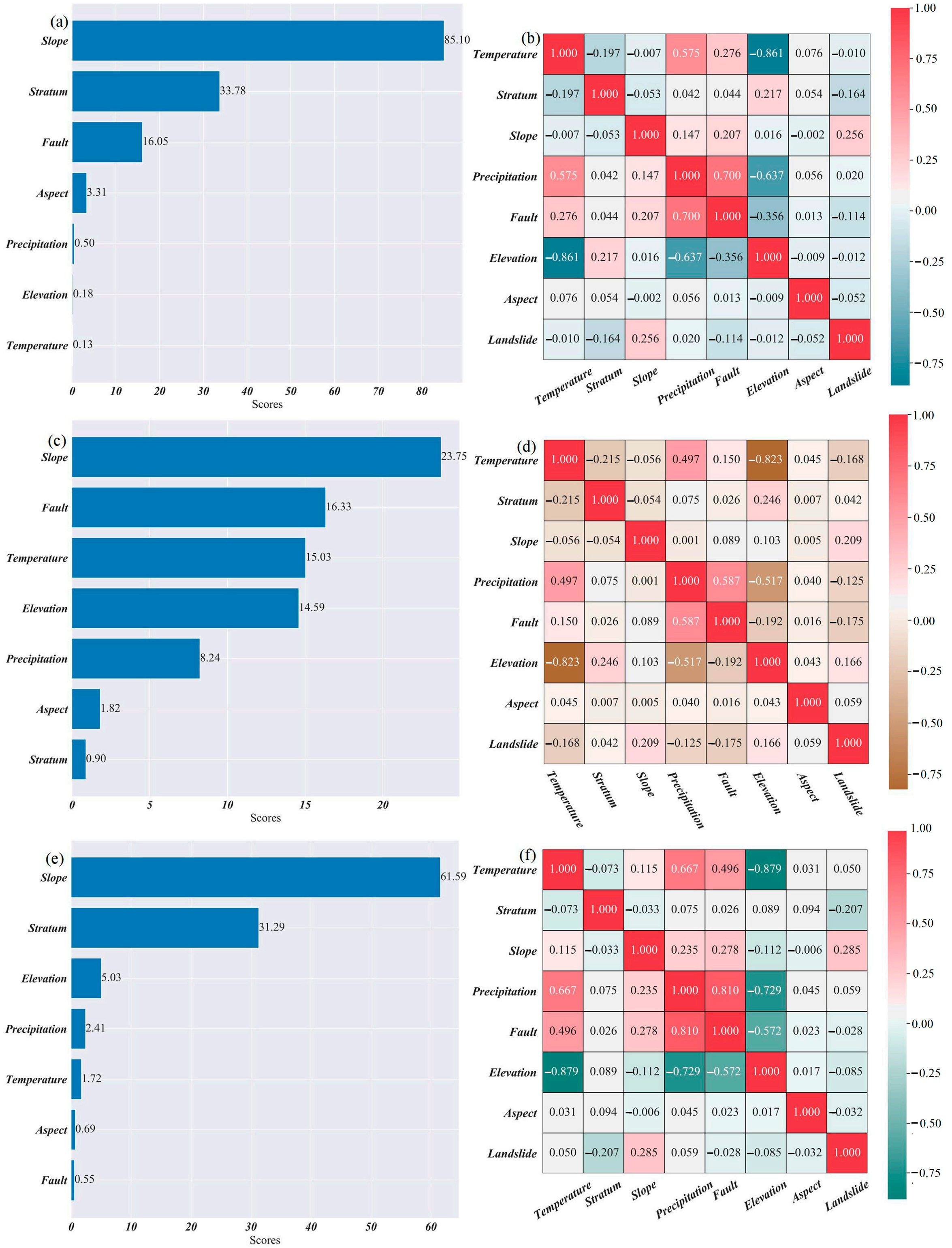

Figure 8. Correlation between landslides and influencing factors. (**a**) Chi-square test between all landslides and influencing factors; (**b**) correlation coefficients between all landslides and influencing factors; (**c**) chi-square test between large and super large landslides and influencing factors; (**d**) correlation coefficients between large and super large landslides and influencing factors; (**e**) chi-square test between medium and small landslides and influencing factors; (**f**) correlation coefficients between medium and small landslides and influencing factors.

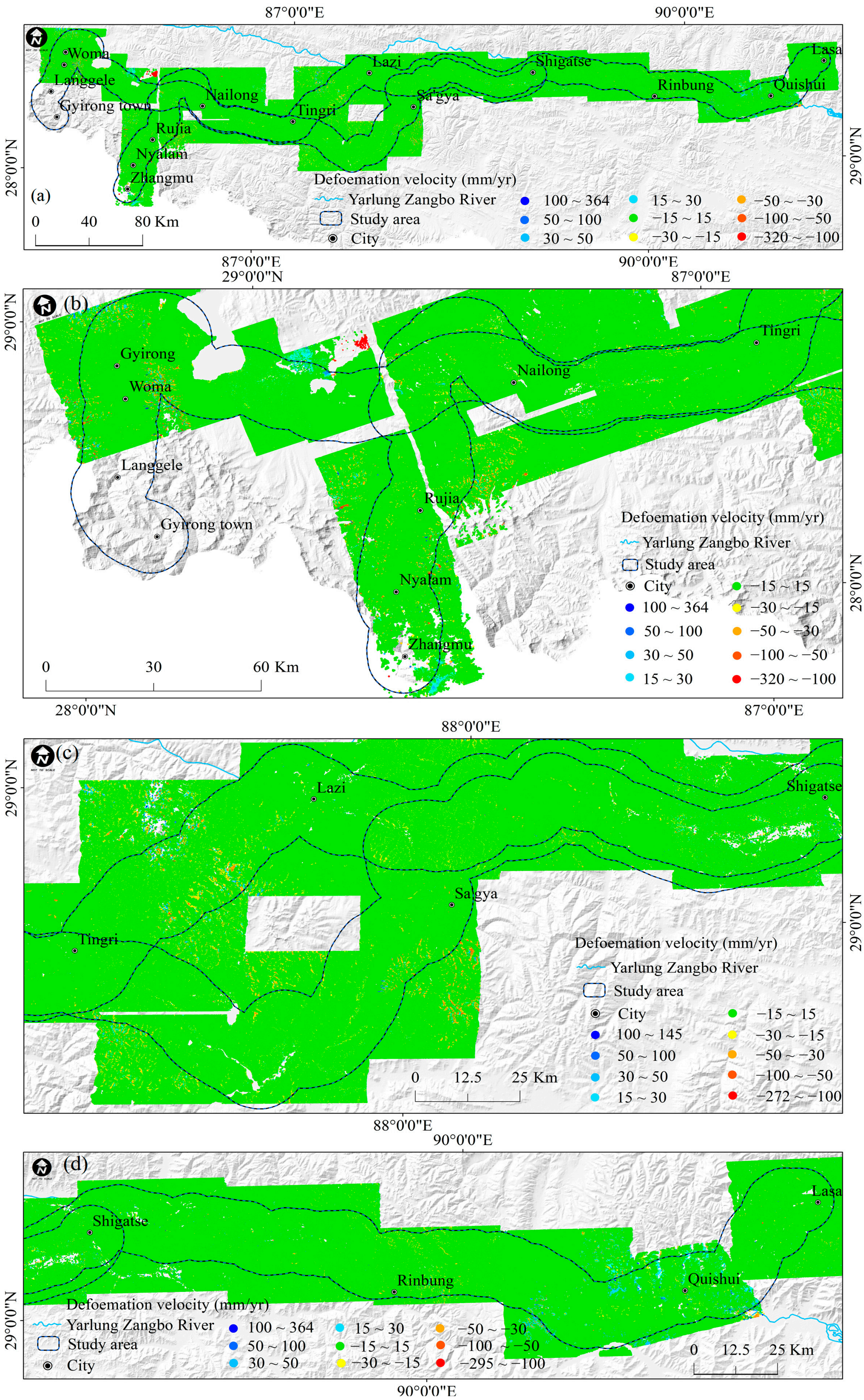

Figure 9. Ground surface deformation of the China–Nepal transportation corridor. (**a**) Shows the entire study area's ground surface deformation; (**b**) the sections from Gyirong and Zhangmu Town to Dingri; (**c**) the section from Dingri to Shigatse; (**d**) the section from Shigatse to L.

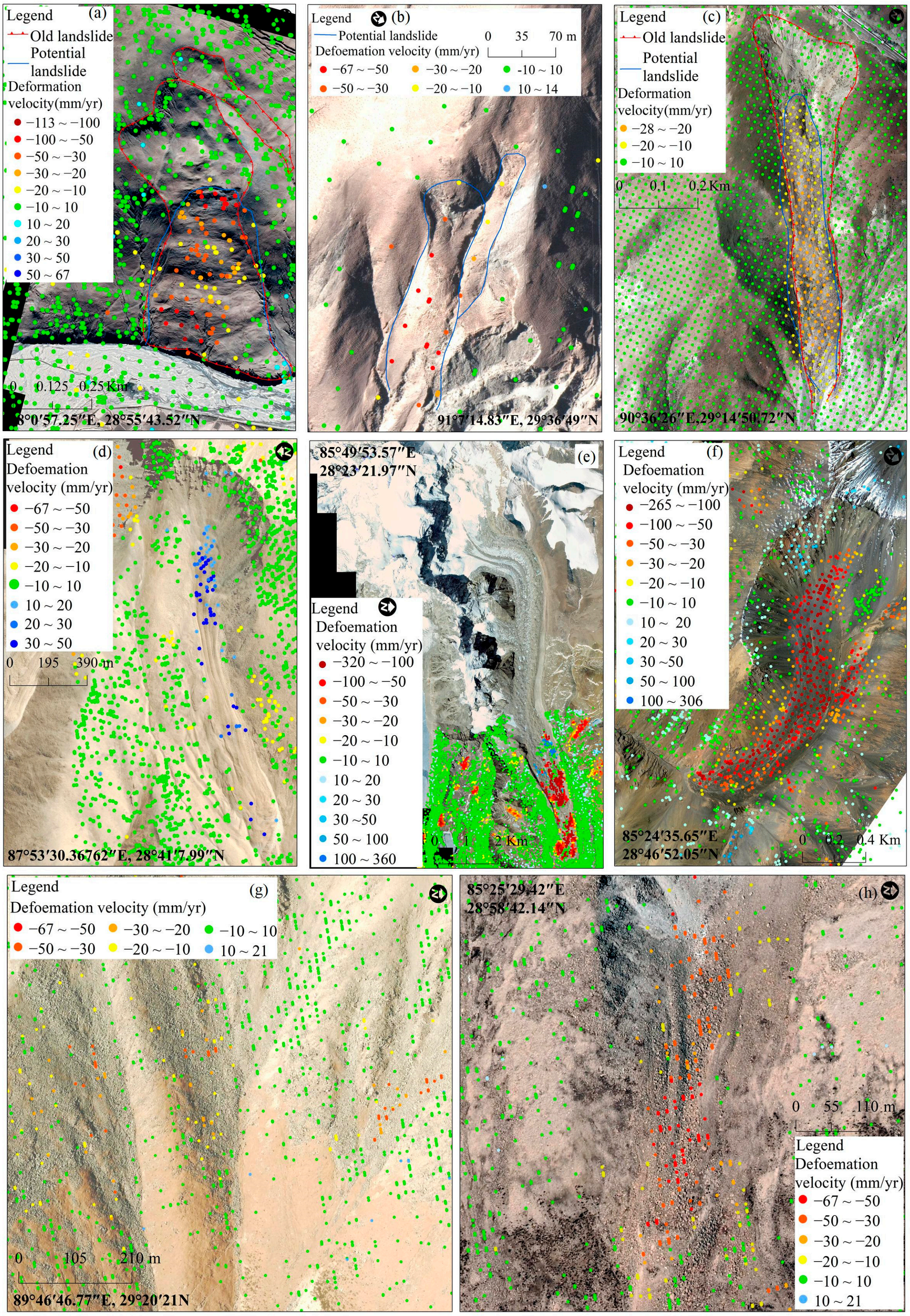

Figure 10. Typical ground surface deformation types along the China–Nepal transportation corridor. (**a**–**c**) potential landslides; (**d**–**f**) glacier movement; (**g**,**h**) slope weathering layer.

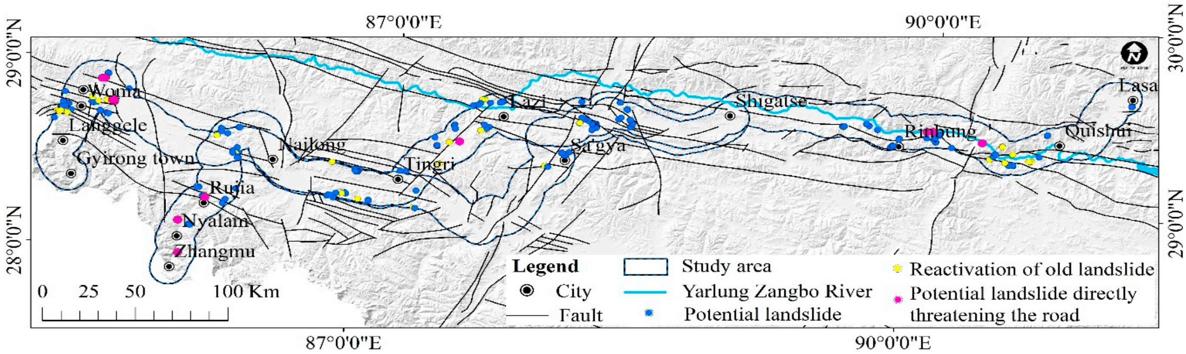

Figure 11. Spatial distribution of potential landslides.

5. Discussion

Causes of Landslides

The study area may still be in a relatively active tectonic environment, with the direction of tectonic stress being north-northeast and the distributions of directions and rates of tectonic stress being generally consistent between different regions in the area (Figure 12) [20,76]. Tectonic stress affects faults and seismicity [77]. Statistics indicate that earthquake landslide disasters can be triggered when the earthquake magnitude (M_L) is greater than 4.0 [78]. Since 1980, there have been a total of 3090 earthquakes and 103 earthquakes with magnitudes greater than 4.0.

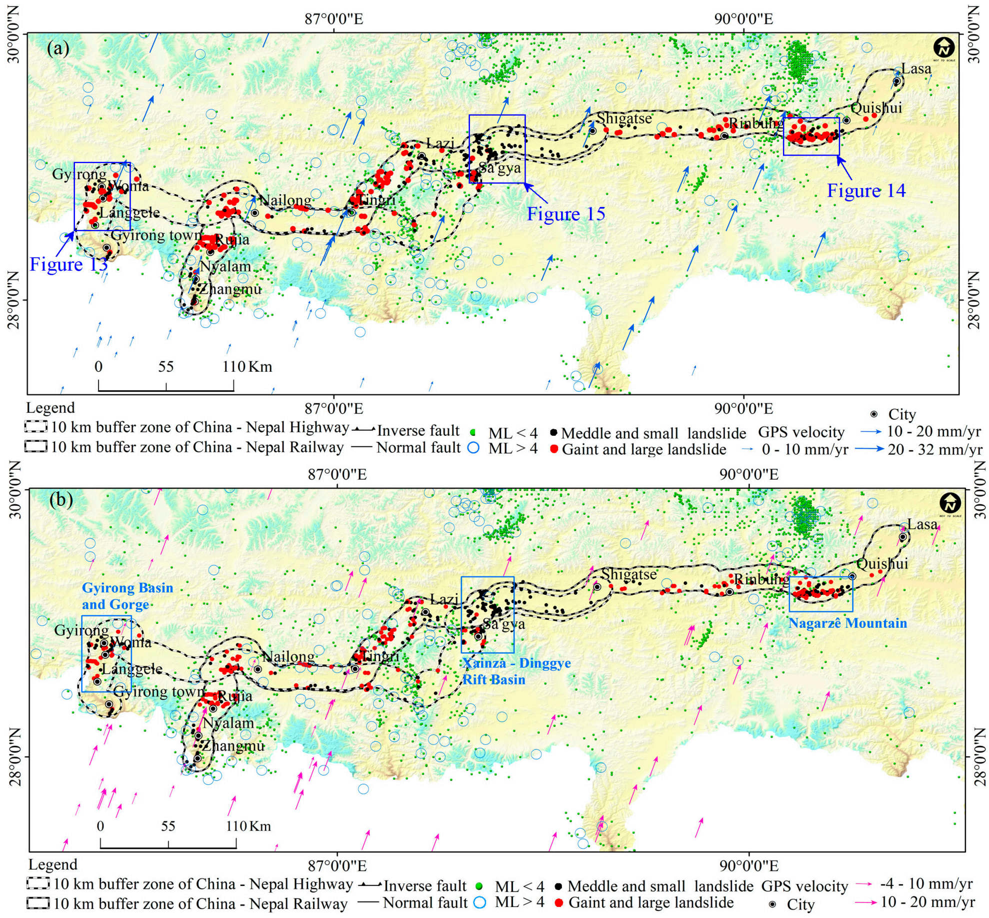

Figure 12. Distribution of historical landslides, tectonic stresses, and earthquakes. (**a**) GPS rate facing north; (**b**) GPS rate facing east (data in the figure are from [20,76]).

The results of the landslide influencing factors in Section 4.3 indicate that all landslides in the area are closely related to slope and are all concentrated in the same slope range. Meanwhile, temperature, elevation, precipitation, aspect, strata, and faults all have significantly different effects on landslides of different sizes. Therefore, in this study, we further discuss the causes of landslides in the region based on the spatial distribution of landslides within the area. By combining the differences in influencing factors for landslides within typical geomorphic units, we further discuss the causes of landslides in the region. The three typical regions are as follows: (1) Gyirong basin and gorge, which is dominated by normal faults and folds (Figure 13); (2) Nagarzê Mountain in Shannan City, which is dominated by thrust faults (Figure 14); and (3) Xainza-Dinggye Rift Basin, where both normal faults and thrust faults are developed (Figure 15).

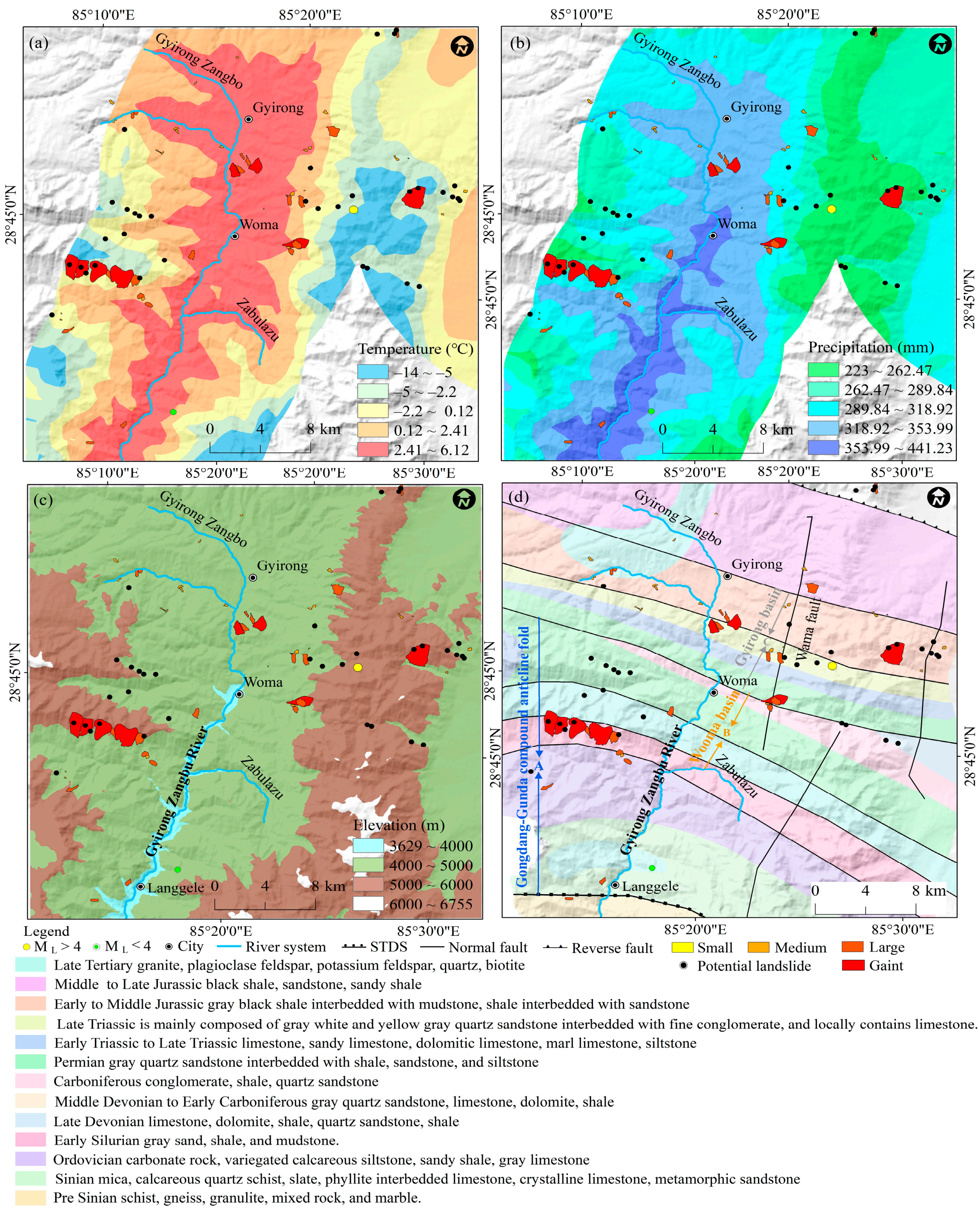

Figure 13. Distribution of landslides in the Gyirong basin and canyon. (**a**) Landslides and temperature; (**b**) landslides and precipitation; (**c**) landslides and altitude; (**d**) Landslides and faults and strata.

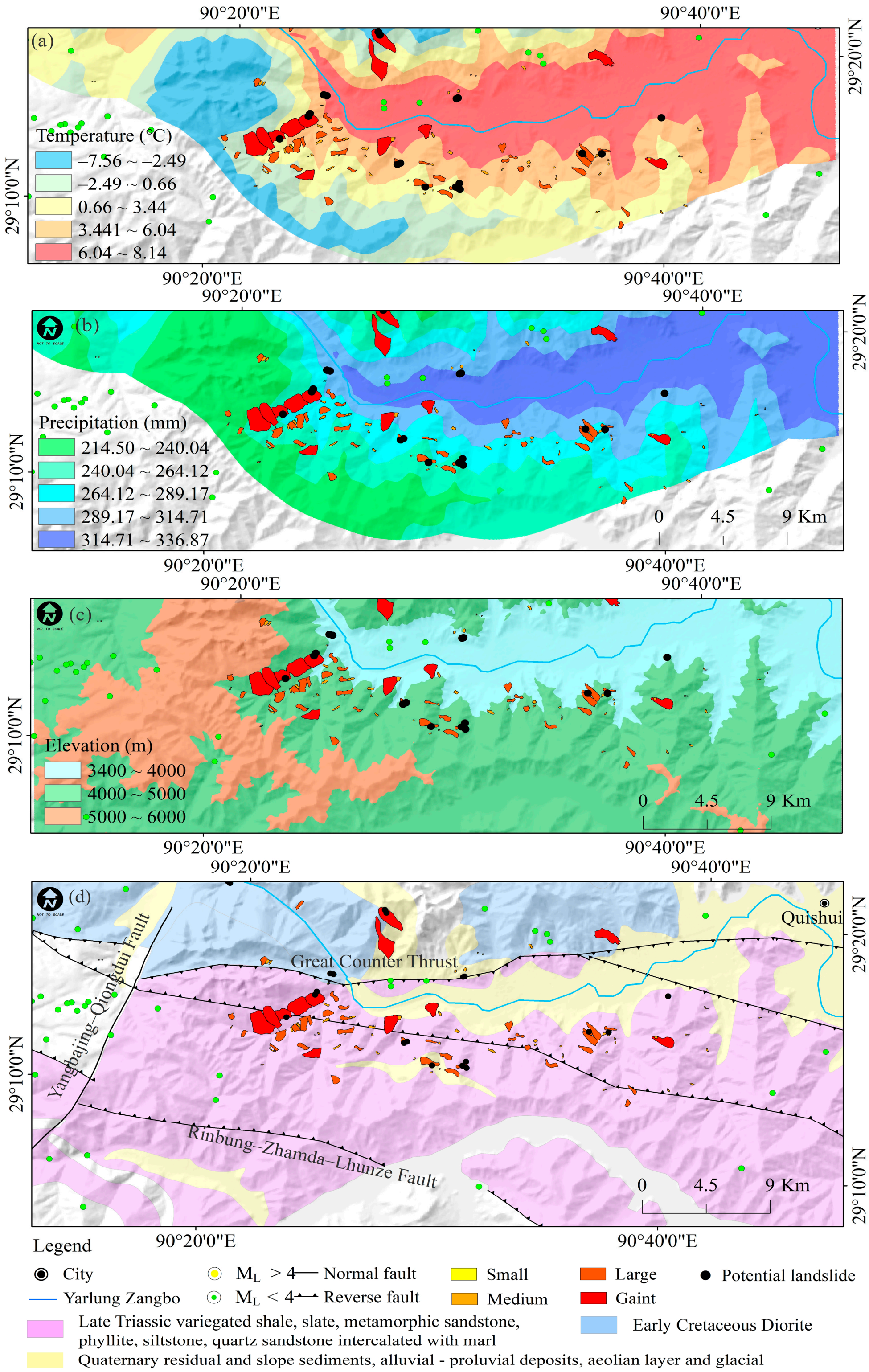

Figure 14. Distribution of landslides in the Nagarzê Mountain. (**a**) Landslides and temperature; (**b**) landslides and precipitation; (**c**) landslides and altitude; (**d**) Landslides and faults and strata. Xainza-Dinggye Rift Basin.

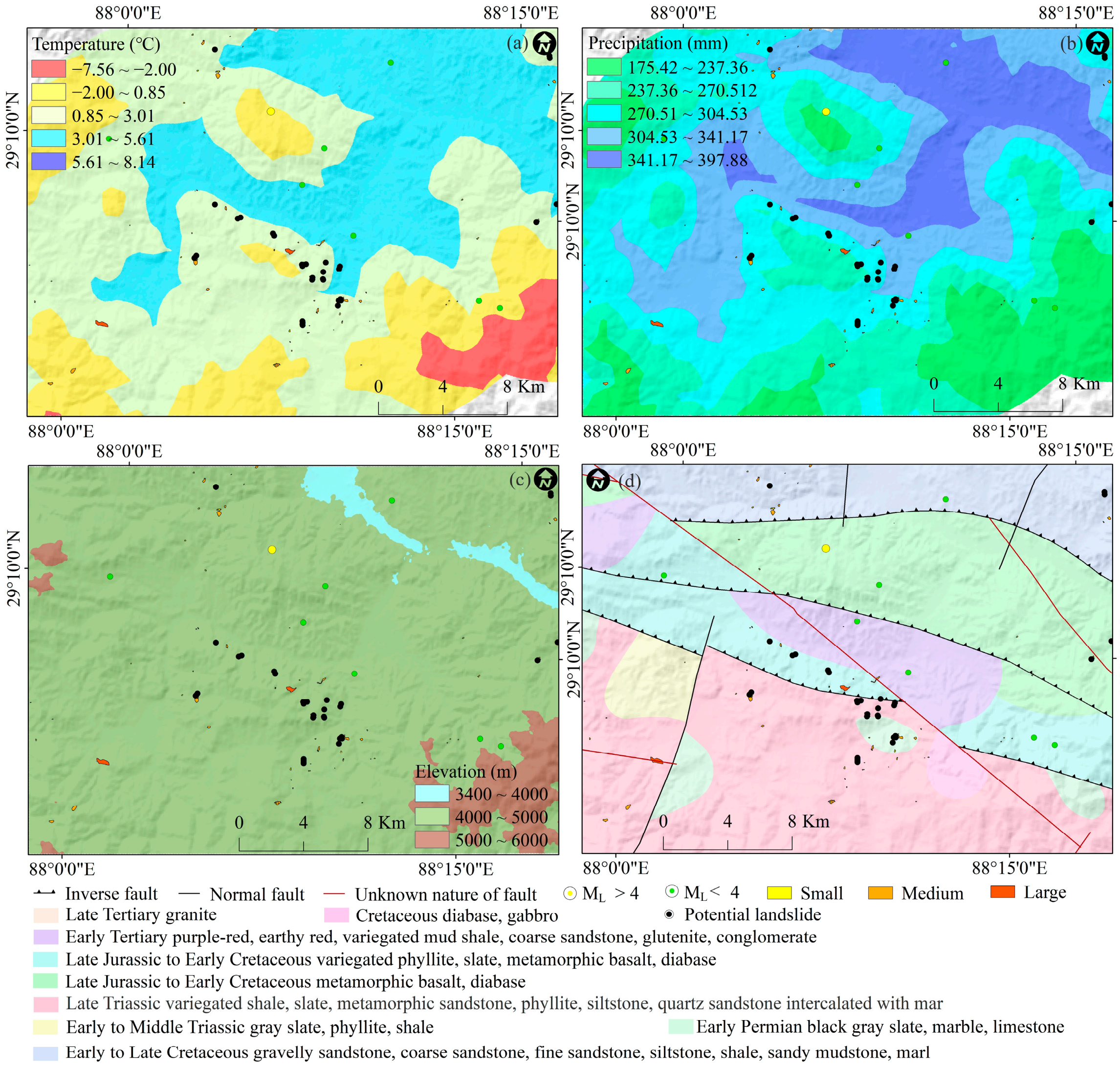

Figure 15. Distribution of landslides in the Xainza-Dinggye Rift Basin. (**a**) Landslides and temperature; (**b**) landslides and precipitation; (**c**) landslides and altitude; (**d**) Landslides and faults and strata.

Gyirong basin and gorge: In this region, both historical and potential landslides show a pattern of decreasing numbers with increasing distance from the fault. In addition, super-large and large landslides are distributed along the fault, and the size of the landslide gradually decreases as the distance from the fault increases (Figure 13). On the west side of the Gyirong Zangbu River, south of the Woma to Langgele region, is a 30 km-wide Gongdang-Gunda compound anticline fold structure (Zone A) [79]. Landslides in this area occurred along the fault in the relatively weak sandstone, shale, and marl strata. On the east side of the Gyirong Zangbu River, Zabraqu to Wooma, and Gyirong County to Wooma are the Wooma and Gyirong basins (Zones B and C, respectively). The high-angle Wooma Eastern normal fault developed on the east side of this region [80], and historical landslides mainly developed in the relatively weak Jurassic shale and mudstone interbedded strata (Figure 13d). In addition to being distributed in the aforementioned strata, potential landslides also occur in relatively hard quartz sandstone interbedded with shale, sandstone, and siltstone. On the various landforms, brittle normal faults that formed under gravity slump have developed [80]. Near the fault zone, the rock mass structural plane is densely developed, with a high degree of fragmentation and poor geotechnical physical properties [60,81], and there is reduced slope stability. From the mountaintop to the valley, the number of historical and potential landslides in the region does not always increase with rising temperatures (Figure 13a). This indicates that high temperatures do not necessarily have an absolute promoting effect on landslide development, and they may also be influenced by other factors. Furthermore, the number of landslides in this region did not increase with increasing precipitation (Figure 13b). Instead, the distribution of super-large, large, and potential landslides is in areas with less precipitation at high altitudes (above 5000 m) (Figure 13c). This may be due to the fact that in high-altitude areas, the air is thinner and there is intense solar radiation, leading to more intense external erosion on slopes. In particular, the anticlinal fold structure in Zone A is susceptible to weathering and produces joints and fissures. Meltwater from ice and snow infiltrates along the fractured structural plane, decreasing the cohesion of the rock and soil mass, thereby affecting the integrity of the rock mass structure [82]. In conclusion, besides the influence of slope gradient, the combined effects of faulting, altitude, and relatively weak strata result in the distribution of historical and potential landslides along faults and ridges in this region. This phenomenon is more pronounced in the distribution of super-large and large landslides.

Nagarzê Mountain is in Shannan City. Both landslides of various sizes and potential landslides in the area are distributed along the fault (Figure 14d). The development of landslides in this area depends on the tectonic environment (Figure 10). First, the region has developed a series of thrust faults arranged in a layered tile pattern [83]. The Tethys Himalayan Strata have overlain the Yarlung Zangbo River Ophiolite Belt in a northward direction under thrust [84], resulting in a significant hanging-wall effect. The thrust of the fault causes stress concentration in the hanging wall, resulting in more joint fractures and weak structural planes near the fault [85,86]. Moreover, this region is located near the Yarlung Zangbo Suture Zone, with the Lhasa block to the north, the Himalaya block to the south, and the Yangbajing-Qiongdui fault to the west. The regional tectonic stress is concentrated at about 2 kpa/yr (compared with a general tectonic stress of about 1 kpa/yr in other regions), and the material structure is fractured [77,87]. Furthermore, this region is characterized by relatively weak Triassic Langxuejie Group sedimentary strata, which mainly consist of slate, phyllite, siltstone, and quartz sandstone with marl [88]. In addition, landslides are almost exclusively distributed above 0 °C, indicating that regions with higher temperatures are more conducive to the development of landslides (including potential landslides) compared to colder areas (Figure 14a). It is worth noting that super-large and large landslides are predominantly developed within the range of 4000–5000 m (Figure 14b), which is consistent with the relationship between landslides and elevation described in Section 4.3. The above analysis indicates that in high-altitude areas, the combined effect of intense solar radiation and higher temperatures influences the weathering of the relatively weak rock layers in this region, thereby weakening the strength of the slope's soil and rock. In addition, the number of historic and potential landslides in this region did not decrease with a decrease in precipitation (Figure 14c). This suggests that an increase in rainfall does not necessarily lead to landslides or deformation, especially in the development of large and very large landslides. In conclusion, landslides in this region are the result of the combined effects of faulting, temperature, elevation, and strata. However, faults and strata have a greater influence on landslides in this area. Therefore, the hanging-wall effect of the thrust fault and the soft material composition of the strata promote the development of landslides in this region.

This region is dominated by small and medium-sized landslides, and their spatial distribution is highly random, while a limited number of large landslides occur predominantly near faults (Figure 11). Favorable strata provide a critical foundation for landslides. This region consists of a series of sedimentary layers of relatively weak lithology that are easily eroded or disturbed by external forces. Historical and potential landslides are mainly distributed on variegated shale, slate, metamorphic sandstone, fine-grained quartz sandstone, marl-stone, grayish-black shale, limestone, fine sandstone, siltstone, sandstone, phyllite, and sandy mudstone. In addition, this area is a complex tectonic environment at the intersection of the north-south normal fault (which has been relatively active since the Quaternary) [89] and the east-west thrust fault. Although earthquakes of magnitudes less than four are difficult to induce landslides directly, frequent earthquakes can cause cumulative damage and affect the integrity of the rock mass structure [90], and this effect is more pronounced in strata with relatively weak rock properties [91]. The number of historical and potential landslides does not show a clear pattern of increase or decrease with increasing temperature and precipitation. Instead, they are concentrated in regions where strata are relatively weak and both precipitation and temperatures are moderate (Figure 15a,b). Therefore, under favorable strata conditions, temperature and precipitation may contribute to the development of landslides but are not the dominant factors. Furthermore, we found that the landslides (including potential landslides) in this region are all developed within the elevation range of 4000–5000 m (Figure 15c). This is due to the high-altitude base of the Qinghai–Tibet Plateau and the topography of the Xainza-Dinggye Rift Basin. Therefore, the contribution of elevation to landslides in this region may be consistent. In summary, the combined effects of relatively weak material composition and the cumulative damage from earthquakes contribute to the development of small and medium-sized landslides in the area.

6. Conclusions

This paper takes the China–Nepal traffic corridor as its research area, presents a landslide distribution map, and determines the controlling factors and causes of landslide development. Based on the distribution of potential landslides, potential landslip hazard areas are determined. The results of this study lead to the following new understandings:

The following are the regional spatial distribution characteristics of 609 historical landslides. First, they are mainly distributed along faults. Second, they have the characteristics of overall dispersion and local accumulation and are mainly concentrated in the Gyirong basin and gorge, the Lazi-Tingri Mountain, and the Nagarzê Mountain in Shannan City (these three regions develop super-large and large landslides) and the Xainza-Dinggye Rift Basin (this region is conducive to small and medium-sized landslides). In general, landslides in the region are distributed along faults and mainly develop in weak and relatively weak strata within 2 km of faults, on slope angles between 20° and 30°, with south to southwest slope aspects, and at elevations between 4000 and 5000 m.

We determined the relationship between landslide area and volume for the region and found that the area of historical landslides ranged from 2.78×10^2 m^2 to 2.46×10^6 m^2, and their volume ranged from 1.6×10^3 m^3 to 4.8×10^7 m^3. A total of 47 super-large and 213 large landslides were mainly distributed along faults and ridges. Approximately 349 small and medium-sized landslides mainly developed along gullies. In addition, the correlation between landslides and influencing factors was calculated, and it was found that slope is the most significant influencing factor for landslide development in the area. In addition to the slope, faults significantly influence the development of very large and large landslides (mainly affected by fault activity within 2 km); strata significantly influence the development of small landslides.

Based on 111 scenes of Sentinel-1A data, we used the ITPA method and field investigation to categorize three types of ground movement: moraine movement, ground deformation, and potential landslides. The spatial distribution of the 223 potential landslides that we identified is similar to that of historical landslides. There are fifteen potential landslides that pose a direct threat to traffic arteries, mainly in the Renbu Canyon section of the China–Nepal Highway and the proposed China–Nepal Railway (Pekucuo to Gyirong County section).

Based on the size of landslides within the area and considering the differences in factors other than slope within typical geomorphic units, we further discussed the causes of landslides in different regions. First, the combined effects of faulting, elevation, and relatively weak rock layers have resulted in the distribution of super-large, large, and potential landslides along the ridges and faults in the Gyirong basin and canyon. Second, under the combined influence of the hanging-wall effect of thrust faults and a relatively weak material composition, landslides of various sizes are densely developing in the Nagarzê Mountain of Shannan City. Third, in the Xainza-Dinggye Rift Basin, the relatively weak strata and cumulative damage effects of earthquakes led to the development of small and medium-sized landslides.

Author Contributions: S.Z.: Conceptualization, Software, Methodology, Investigation, Resources, Writing—original draft, Writing—reviewing and editing, Funding acquisition; R.Z.: Supervision, Project administration, Funding acquisition, Writing—reviewing and editing; Z.Z.: Supervision, Methodology, Writing—reviewing and editing, Funding acquisition; X.M.: Supervision, Project administration, Resources; T.Q.: Conceptualization, Software, Writing—reviewing and editing, Supervision; Z.L.: Investigation, Resources; W.G.: Investigation, Resources; G.S.: Resources. All authors have read and agreed to the published version of the manuscript.

Funding: This work was funded by the Second Tibetan Plateau Scientific Expedition and Research Program (STEP) (2021QZKK0204), the Central Guiding Local Science and Technology Development Fund Projects (23ZYQA0326), the Key R&D Program of Gansu Province (22YF7FA021), and the Fundamental Research Funds for the Central Universities (lzujbky-2022-03, lzujbky-2022-it35, and lzujbky-2023-it05).

Data Availability Statement: The data pertaining to this scientific research are currently unavailable for public access due to confidentiality constraints. For inquiries regarding access to the data, please get in touch with the corresponding author.

Acknowledgments: I would like to thank Yan Zhao for his help with the section on the quantitative analysis of landslides and influencing factors.

Conflicts of Interest: The authors declare no conflicts of interest.

References

1. Petley, D.N. Global patterns of loss of life from landslides. *Geology* **2012**, *40*, 927–930. [CrossRef]
2. Zhang, M.; Nie, L.; Xu, Y.; Dai, S. A thrust load-caused landslide triggered by excavation of the slope toe: A case study of the Chaancun Landslide in Dalian City, China. *Arab. J. Geosci.* **2015**, *8*, 6555–6565. [CrossRef]
3. Yin, G.; Luo, J.; Niu, F.; Lin, Z.; Liu, M. Machine learning-based thermokarst landslide susceptibility modeling across the permafrost region on the Qinghai-Tibet Plateau. *Landslides* **2021**, *18*, 2639–2649. [CrossRef]
4. Zhang, Z.; Zeng, R.; Meng, X.; Zhao, S.; Wang, S.; Ma, J.; Wang, H. Effects of changes in soil properties caused by progressive infiltration of rainwater on rainfall-induced landslides. *Catena* **2023**, *233*, 107475. [CrossRef]
5. Zhang, Z.; Zeng, R.; Zhao, S.; Meng, X.; Ma, J.; Yin, H.; Long, Z. Effects of irrigation projects on the classification of yellow river terrace landslides and their failure modes: A case study of heitai terrace. *Remote Sens.* **2023**, *15*, 2015. [CrossRef]
6. Roback, K.; Clark, M.; West, A.; Zekkos, D.; Li, G.; Gallen, S.; Chamlagain, D.; Godt, J. The size, distribution, and mobility of landslides caused by the 2015 M(w)7.8 Gorkha earthquake, Nepal. *Geomorphology* **2018**, *301*, 121–138. [CrossRef]
7. Fan, W.; Lv, J.; Cao, Y.; Shen, M.; Deng, L.; Wei, Y. Characteristics and block kinematics of a fault-related landslide in the Qinba Mountains, western China. *Eng. Geol.* **2019**, *249*, 162–171. [CrossRef]
8. Shang, Y.; Hyun, C.; Park, H.; Yang, Z.; Yuan, G. The 102 Landslide: Human–slope interaction in SE Tibet over a 20-year period. *Environ. Earth Sci.* **2017**, *76*, 47. [CrossRef]
9. Chen, Z.; Zhou, H.; Ye, F.; Liu, B.; Fu, W. The characteristics, induced factors, and formation mechanism of the 2018 Baige landslide in Jinsha River, Southwest China. *Catena* **2021**, *203*, 105337. [CrossRef]
10. Zhou, H.; Liu, B.; Ye, F.; Fu, W.; Tang, W.; Qin, Y.; Fang, T. Landslide distribution and sliding mode control along the Anninghe fault zone at the eastern edge of the Tibetan Plateau. *J. Mt. Sci.* **2021**, *18*, 2094–2107. [CrossRef]
11. Zhao, B.; Li, W.; Wang, Y.; Lu, J.; Li, X. Landslides triggered by the Ms 6.9 Nyingchi earthquake, China (18 November 2017): Analysis of the spatial distribution and occurrence factors. *Landslides* **2019**, *16*, 765–776. [CrossRef]
12. Martha, T.; Roy, P.; Mazumdar, R.; Govindharaj, K.; Kumar, K. Spatial characteristics of landslides triggered by the 2015 M w 7.8 (Gorkha) and M w 7.3 (Dolakha) earthquakes in Nepal. *Landslides* **2017**, *14*, 697–704. [CrossRef]
13. Dortch, J.; Owen, L.; Haneberg, W.; Caffee, M.; Dietsch, C.; Kamp, U. Nature and timing of large landslides in the Himalaya and Transhimalaya of northern India. *Quat. Sci. Rev.* **2009**, *28*, 1037–1054. [CrossRef]
14. Du, G.; Zhang, Y.; Yao, X.; Yang, Z.; Yuan, Y. Field investigations and numerical modeling of a giant landslide in the region of Eastern Himalayan Syntaxis: Jiaobunong landslide. *J. Mt. Sci.* **2021**, *18*, 3230–3232. [CrossRef]
15. Gong, Y.; Yao, A.; Li, Y.; Li, Y.; Tian, T. Classification and distribution of large-scale high-position landslides in southeastern edge of the Qinghai–Tibet Plateau, China. *Environ. Earth Sci.* **2022**, *81*, 311. [CrossRef]
16. Zhou, J.; Cui, P.; Hao, M. Comprehensive analyses of the initiation and entrainment processes of the 2000 Yigong catastrophic landslide in Tibet, China. *Landslides* **2016**, *13*, 39–54. [CrossRef]

17. Zhang, Y.; Chen, J.; Zhou, F.; Bao, Y.; Yan, J.; Zhang, Y.; Li, Y.; Gu, F.; Wang, Q. Combined numerical investigation of the Gangda paleolandslide runout and associated dam breach flood propagation in the upper Jinsha River, SE Tibetan Plateau. *Landslides* **2022**, *19*, 941–962. [CrossRef]
18. Guo, J.; Cui, Y.; Xu, W.; Shen, W.; Li, T.; Yi, S. A novel friction weakening-based dynamic model for landslide runout assessment along the Sichuan-Tibet Railway. *Eng. Geol.* **2022**, *365*, 106721. [CrossRef]
19. Yin, A.; Harrison, T. Geologic Evolution of the Himalayan–Tibetan Orogen. *Annu. Rev. Earth Planet. Sci.* **2000**, *28*, 211–280. [CrossRef]
20. Zheng, G.; Wang, H.; Wright, T.; Lou, Y.; Zhang, R.; Zhang, W.; Shi, C.; Huang, J.; Wei, N. Crustal deformation in the India-Eurasia collision zone from 25 years of GPS measurements. *J. Geophys. Res. Solid Earth* **2017**, *122*, 9290–9312. [CrossRef]
21. Meng, W.; Guo, C.; Mao, B.; Lu, H.; Chen, Q.; Xu, X. Tectonic Stress Field and Engineering Influence of China—Nepal Railway Corridor. *Geoscience* **2020**, *35*, 167–179.
22. Jia, Y.; Liu, J.; Guo, L.; Deng, Z.; Li, J.; Zheng, H. Locomotion of Slope Geohazards Responding to Climate Change in the Qinghai-Tibetan Plateau and Its Adjacent Regions. *Sustainability* **2021**, *13*, 10488. [CrossRef]
23. Wu, Z.; Barosh, P.; Ha, G.; Yao, X.; Xu, Y.; Liu, J. Damage induced by the 25 April 2015 Nepal earthquake in the Tibetan border region of China and increased post seismic hazards. *Nat. Hazard Earth Syst. Sci.* **2019**, *19*, 873–888. [CrossRef]
24. Ma, F.; Li, Z.; Wang, J.; Kuo, D. Monitoring and engineering geology analysis of the Zhangmu landslide in Tibet, China. *Bull. Eng. Geol. Environ.* **2017**, *76*, 855–873. [CrossRef]
25. Guo, M.; Liu, S.; Yin, S.; Wang, S. Stability analysis of the Zhangmu multi-layer landslide using the vector sum method in Tibet, China. *Bull. Eng. Geol. Environ.* **2019**, *78*, 4187–4200. [CrossRef]
26. Han, D.; Yang, C.; Dong, J. InSAR monitoring and analysis of landslide deformation after the earthquake in the Zhangmu port, Tibet. *J. Geomech.* **2020**, *26*, 565–574.
27. Han, P.; Wang, M.; Jiang, Z.; Fan, X.; Tian, S. Geological disasters and their influencing factors in Jilong County, Tibet. *Chin. J. Geol. Hazard Control* **2020**, *31*, 111–118.
28. Xiong, D.; Cui, X. The relationship between main geological hazard and topography in the Himalayan seismic belt: A case study in the Xigaze area, Tibet. *Geol. Bull. China* **2021**, *40*, 1967–1980.
29. Fu, M.; Zhan, T.; Xu, C. Characteristics and Developmental Laws of Geological Hazards along G318 Lhasa-Shigatse. *J. Seismol. Res.* **2019**, *42*, 438–446+456.
30. Li, T. The process and mechanism of the rise of the Qinghai-Tibet Plateau. *Tectonophysics* **1996**, *260*, 45–53. [CrossRef]
31. Yin, A. Cenozoic tectonic evolution of the Himalayan orogen as constrained by along-strike variation of structural geometry, exhumation history, and foreland sedimentation. *Earth Sci. Rev.* **2006**, *76*, 1–131. [CrossRef]
32. Zhu, D.; Zhao, Z.; Niu, Y.; Dilek, Y.; Hou, Z.; Mo, X. The origin and pre enozoic evolution of the Tibetan Plateau. *Gondwana Res.* **2013**, *23*, 1429–1454. [CrossRef]
33. Zhu, D.; Zhao, Z.; Niu, Y.; Dilek, Y.; Mo, X. Lhasa terrane in southern Tibet came from Australia. *Geology* **2011**, *39*, 727–730. [CrossRef]
34. Yin, A. Mode of Cenozoic east-west extension in Tibet suggesting a common origin of rifts in Asia during the Indo-Asian collision. *J. Geophys. Res.-Solid Earth* **2000**, *105*, 21745–21759. [CrossRef]
35. Zhang, J.; Santosh, M.; Wang, X.; Guo, L.; Yang, X.; Zhang, B. Tectonics of the northern Himalaya since the India–Asia collision. *Gondwana Res* **2012**, *21*, 939–960. [CrossRef]
36. Zhang, J.; Guo, L. Structure and geochronology of the southern Xainza–Dinggye rift and its relationship to the south Tibetan detachment system. *J. Asian. Earth. Sci* **2007**, *29*, 722–736. [CrossRef]
37. Wang, H.; Wright, T.; Zeng, J.; Peng, L. Strain rate distribution in south-central Tibet fromtwo-decades of InSAR and GPS. *Geophys. Res. Lett.* **2019**, *46*, 5170–5179. [CrossRef]
38. Taylor, M.; Yin, A. Active structures of the Himalayan-Tibetan orogen and their relationships to earthquake distribution, contemporary strain field, and Cenozoic volcanism. *Geosphere* **2009**, *5*, 199–214. [CrossRef]
39. He, R.; Gao, R. Some significances of studying north southern rift in Tibet plateau. *Prog. Geophys.* **2003**, *18*, 35–43.
40. Hou, Z.; Gao, Y.; Qu, X.; Rui, Z.; Mo, X. Origin of adakitic intrusives generated during mid-Miocene east–west extension in southern Tibet. *Earth Planet Sci. Lett.* **2004**, *220*, 139–155. [CrossRef]
41. Liao, Q.; Li, D.; Lu, L.; Yuan, Y.; Chu, L. Paleoproterozoic granitic gneisses of the Dinggye and LhagoiKangri areas from the higher and northern Himalaya, Tibet: Geochronology and implications. *Sci. China Earth Sci.* **2008**, *51*, 240–248. [CrossRef]
42. Kang, Z.; Xu, J.; Wilde, S.; Feng, Z.; Chen, J.; Wang, B.; Fu, W.; Pan, H. Geochronology and geochemistry of the Sangri Group Volcanic Rocks, Southern Lhasa Terrane: Implications for the early subduction history of the Neo-Tethys and Gangdese Magmatic Arc. *Lithos* **2014**, *200–201*, 157–168. [CrossRef]
43. Leier, A.; Kapp, P.; Gehrels, G.; DeCelles, P. Detrital zircon geochronology of arboniferous–Cretaceous strata in the Lhasa Terrane, Southern Tibet. *Basin Res.* **2007**, *9*, 361–378. [CrossRef]
44. Yu, X.; Lv, X.; Cao, H. Geochemistry and detrital zircon U-Pb Geochronology of the Triassic nieru formation in the eastern Himalayas and its tectonic implications. *Min. Pet.* **2021**, *41*, 95–108.
45. Liu, G.; Einsele, G. Sedimentary history of the Tethyan basin in the Tibetan Himalayas. *Geol. Rundsch.* **1994**, *83*, 32–61. [CrossRef]
46. Chen, N.; Liu, M.; Deng, M.; Iqbal, J.; Hu, G.; Wahid, S.; Liu, W.; Han, D. The incision variations of Poiqu documented by the Zhangmu landslide in the Upper Himalaya of Tibet. *Quat. Int.* **2019**, *532*, 66–74. [CrossRef]

47. Galli, M.; Ardizzone, F.; Cardinali, M.; Guzzetti, F.; Reichenbach, P. Comparing landslide inventory maps. *Geomorphology* **2008**, *94*, 268–289. [CrossRef]
48. Mondini, A.; Guzzetti, F.; Reichenbach, P.; Rossi, M.; Cardinal, M.; Ardizzone, F. Semi-automatic recognition and maping of rainfall induced shallow landslides using optical satellite images. *Remote Sens. Environ.* **2011**, *115*, 1743–1757. [CrossRef]
49. Salvati, P.; Balducci, V.; Bianchi, C.; Guzzetti, F.; Tonelli, G. A WebGIS for the dissemination of information on historical landslides and floods in Umbria, Italy. *GeoInformatica* **2009**, *13*, 205–322. [CrossRef]
50. Pike, R. The geometric signature: Quantifying landslide-terrain types from digital elevation models. *Math. Geol.* **1988**, *20*, 491–511. [CrossRef]
51. Guzzetti, F.; Mondini, A.; Cardinali, M.; Fiorucci, F.; Santangelo, M.; Chang, K. Landslide inventory maps: New tools for an old problem. *Earth Sci. Rev.* **2012**, *112*, 42–66. [CrossRef]
52. Malamud, B.; Turcotte, D.; Guzzetti, F.; Reichenbach, P. Landslide inventories and their statistical properties. *Earth Surf. Process. Landf.* **2004**, *29*, 687–711. [CrossRef]
53. Guzzetti, F.; Ardizzone, F.; Cardinali, M.; Rossi, M.; Valigi, D. Landslide volumes and landslide mobilization rates in Umbria, central Italy. *Earth Planet Sci. Lett.* **2009**, *279*, 222–229. [CrossRef]
54. Larsen, I.; Montgomery, D.; Korup, O. Landslide erosion controlled by hillslope material. *Nat. Geosci.* **2010**, *3*, 247–251. [CrossRef]
55. Zhang, Y.; Meng, X.; Dijkstra, T. Forecasting the magnitude of potential landslides based on InSAR techniques. *Remote Sens. Environ.* **2020**, *241*, 111738. [CrossRef]
56. Zhang, L.; Dai, K.; Deng, J.; Ge, B.; Liang, R.; Li, W.; Xu, Q. Identifying potential landslides by stacking-InSAR in southwestern China and its performance comparison with SBAS-InSAR. *Remote Sens.* **2021**, *13*, 3662. [CrossRef]
57. Zhao, S.; Zeng, R.; Zhang, H.; Meng, X.; Zhang, Z.; Meng, X.; Wang, H.; Zhang, Y.; Liu, J. Impact of water level fluctuations on landslide deformation at Longyangxia reservoir, Qinghai province, China. *Remote Sens.* **2022**, *14*, 212. [CrossRef]
58. Werner, C.; Wegmuller, U.; Strozzi, T.; Wiesmann, A. Interferometric point target analysis for deformation mapping. *IEEE Int. Geosci. Remote Sens. Symp.* **2003**, *7*, 4362–4364.
59. Hooper, A.; Zebker, H.; Segall, P.; Kampes, B. A new method for measuring deformation on volcanoes and other natural terrains using InSAR persistent scatterers. *Geophys. Res. Lett.* **2004**, *31*. [CrossRef]
60. Guo, C.; Zhang, Y.; Montgomery, D.; Du, Y.; Zhang, G.; Wang, S. How unusual is the long-runout of the earthquake-triggered giant Luanshibao landslide, Tibetan Plateau, China? *Geomorphology* **2016**, *259*, 145–154. [CrossRef]
61. Qi, T.; Meng, X.; Qing, F.; Zhao, Y.; Shi, W.; Chen, G.; Zhang, Y.; Li, Y.; Yue, D.; Su, X.; et al. Distribution and characteristics of large landslides in a fault zone: A case study of the NE Qinghai-Tibet Plateau. *Geomorphology* **2021**, *379*, 107592. [CrossRef]
62. Collettini, C.; Niemeijer, A.; Viti, C.; Marone, C. Fault zone fabric and fault weakness. *Nature* **2009**, *462*, 907–910. [CrossRef]
63. Meng, X.; Chen, G.; Guo, P.; Xiong, M.; Wasowski, J. Research of landslide and debris flows in Bailong River basin: Progress and prospect. *Mar. Geol. Quat. Geol.* **2013**, *33*, 1–15. [CrossRef]
64. Valagussa, A.; Marc, O.; Frattini, P.; Crosta, G. Seismic and geological controls on earthquake-induced landslide size. *Earth Planet Sci. Lett.* **2019**, *506*, 268–281. [CrossRef]
65. Bui, D.; Tsangaratos, P.; Nguyen, V.; Liem, N.; Trinh, P. Comparing the prediction performance of a Deep Learning Neural Network model with conventional machine learning models in landslide susceptibility assessment. *Catena* **2020**, *188*, 104426. [CrossRef]
66. Kavzoglu, T.; Sahin, E.; Colkesen, I. Landslide susceptibility mapping using GIS-based multi-criteria decision analysis, support vector machines, and logistic regression. *Landslides* **2014**, *11*, 425–439. [CrossRef]
67. Clarke, B.; Burbank, D. Bedrock fracturing, threshold hillslopes, and limits to the magnitude of bedrock landslides. *Earth Planet. Sci. Lett.* **2010**, *297*, 577–586. [CrossRef]
68. Liu, C.; Qi, S.; Tong, L.; An, G.; Li, X. Great landslides in Himalaya mountain area and their occurrence with lithology. *J. Eng. Geol.* **2010**, *18*, 669–676.
69. Zhao, H.; Ma, F.; Li, Z.; Guo, J.; Zhang, J. Geological hazards and protective measures of road slope in Himalaya mountain area. *J. Eng. Geol.* **2022**, *30*, 656–671.
70. Wang, X.; Clague, J.; Crosta, G.; Sun, J.; Stead, D.; Qi, S.; Zhang, L. Relationship between the spatial distribution of landslides and rock mass strength, and implications for the driving mechanism of landslides in tectonically active mountain ranges. *Eng. Geol.* **2021**, *292*, 106281. [CrossRef]
71. Collins, B.; Stock, G. Rockfall triggering by cyclic thermal stressing of exfoliation fractures. *Nat. Geosci.* **2016**, *9*, 395–400. [CrossRef]
72. Rahmati, O.; Pourghasemi, H.; Melesse, A. Application of GIS-based data driven random forest and maximum entropy models for groundwater potential mapping: A case study at Mehran Region, Iran. *Catena* **2016**, *137*, 360–372. [CrossRef]
73. Sun, D.; Wen, H.; Wang, D.; Xu, J. A random forest model of landslide susceptibility map** based on hyperparameter optimization using Bayes algorithm. *Geomorphology* **2020**, *362*, 107201. [CrossRef]
74. Huang, F.; Chen, J.; Liu, W.; Huang, J.; Hong, Y.; Chen, W. Regional rainfall-induced landslide hazard warning based on landslide susceptibility mapping and a critical rainfall threshold. *Geomorphology* **2022**, *408*, 108236. [CrossRef]
75. Patton, A.; Rathburn, S.; Capps, D. Landslide response to climate change in permafrost regions. *Geomorphology* **2019**, *340*, 116–128. [CrossRef]

76. Kreemer, C.; Blewitt, G.; Klein, E. A geodetic plate motion and Global Strain Rate Model. *Geochem. Geophys. Geosyst.* **2014**, *15*, 3849–3889. [CrossRef]
77. Jiang, G.; Xu, C.; Wen, Y.; Xu, Y.; Ding, K.; Wang, J. Contemporary tectonic stressing rates of major strike-slip faults in the Tibetan Plateau from GPS observations using least-squares collocation. *Tectonophysics* **2014**, *615*, 85–95. [CrossRef]
78. Keefer, D. Landslides caused by earthquakes. *Geol. Soc. Am. Bull.* **1984**, *95*, 406–421. [CrossRef]
79. Wang, D.; Zhang, J.; Yang, X.; Qi, G. Tectonic and environmental evolution of Gyirong basin, and its relationship to the uplift of Tibetan plateau. *Acta Sci. Nat. Univ. Pekin.* **2009**, *45*, 79–89.
80. Wang, X.; Zhang, J.; Yang, X. Geochemical characteristics of the leucogranites from Gyirong, south Tibet: Formation mechanism and tectonic implications. *Geotecton. Metallog.* **2017**, *41*, 354–368.
81. Zhang, Y.; Guo, C.; Yao, X.; Yang, Z.; Wu, R.; Du, G. Research on the Geohazard effect of active fault on the eastern marg of the Tibetan Plateau. *Acta. Geol. Sin.* **2016**, *37*, 277–286.
82. Delgado, F.; Zerathe, S.; Schwartz, s.; Mathieux, B.; Benavente, C. Inventory of large landslides along the Central Western Andes (ca. 15°–20° S): Landslide distribution patterns and insights on controlling factors. *J. S. Am. Earth. Sci* **2022**, *116*, 103824. [CrossRef]
83. Yin, A.; Kapp, P.; Murphy, M.; Manning, C.; Harrison, T.; Grove, M.; Wu, C. Significant late Neogene east-west extension in northern Tibet. *Geology* **1999**, *27*, 787–790. [CrossRef]
84. Ratschbacher, L.; Frisch, W.; Liu, G.; Chen, C. Distributed deformation in southern and western Tibet during and after the India-Asia collision. *J. Geophys. Res. Solid Earth* **1994**, *99*, 19917–19945. [CrossRef]
85. Meunier, P.; Hovius, N.; Haines, J. Topographic site effects and the location of earthquake induced landslides. *Earth Planet Sci. Lett.* **2008**, *275*, 221–232. [CrossRef]
86. He, K.; Ma, G.; Hu, X. Formation mechanisms and evolution model of the tectonic-related ancient giant basalt landslide in Yanyuan County, China. *Nat. Hazards* **2021**, *106*, 2575–2597. [CrossRef]
87. Sun, Y.; Guo, C.; Wu, Z.; Fan, T.; Li, H. Numerical study of the crustal stress, strain rate and fault activity in the eastern Tibetan plateau. *Acta Geol. Sin.* **2017**, *38*, 385–392.
88. Zhang, C.; Li, X. Attribution of the Cretaceous Melange along eastern segment of the Yarlung Zangbo suture zone: Implications to tectonics boundary between India and Aisa collision. *Geol. Bull. China* **2015**, *34*, 2236–2245.
89. Wang, H.; Zhang, L.; Yin, K.; Luo, H.; Li, J. Landslide identification using machine learning. *Geosci. Front.* **2021**, *12*, 351–364. [CrossRef]
90. Zhang, Y.; Su, S.; Wu, S.; Shi, J.; Sun, P.; Yao, X.; Xiong, T. Research on relationship between fault movement and large-scale landslide in intensive earthquake region. *Chin. J. Rock Mech. Eng.* **2011**, *30*, 3503–3513.
91. Feng, J.; Zhang, Y.; He, J.; Zhu, H.; Huang, L.; Mao, W.; Fu, H.; Li, D. Dynamic response and failure evolution of low-angled interbedding soft and hard stratum rock slope under earthquake. *Bull. Eng. Geol. Environ.* **2022**, *81*, 400. [CrossRef]

Disclaimer/Publisher's Note: The statements, opinions and data contained in all publications are solely those of the individual author(s) and contributor(s) and not of MDPI and/or the editor(s). MDPI and/or the editor(s) disclaim responsibility for any injury to people or property resulting from any ideas, methods, instructions or products referred to in the content.